Crouzeix-Raviart approximation of the total variation on simplicial meshes

Antonin Chambolle, Thomas Pock

Crouzeix-Raviart approximation of the total variation on simplicial meshes.

Antonin Chambolle*, and Thomas Pock†

May 7, 2018

Abstract

We propose an adaptive implementation of a Crouzeix-Raviart based discretization of the total variation, which has the property of approximating from below the total variation, with metrication errors only depending on the local curvature, rather than on the orientation as is usual for other approaches.

Keywords: Image processing, total variation, nonconforming finite elements (Crouzeix-Raviart).

AMS MSC (2010): 49Q20 26A45 65K10 65N30

1 Introduction

Since [39], the total variation has been widely used in imaging as a basic denoising tool and a regularizer for inverse problems, obviously as it is one of the few convex regularizing energies which preserve discontinuities [14]. Classically, it is defined for a (here, to simplify, scalar) function $u : \Omega \to \mathbb{R}$ defined on a domain $\Omega \subset \mathbb{R}^d$ ($d = 2$ or 3 for most imaging applications) as the (total) varation of the distributional derivative, Du, which is assumed to be a measure. An equivalent definition, by duality, is simply

$$|Du|(\Omega) = \sup \left\{ -\int_\Omega u(x) \mathrm{div}\, \varphi(x) dx : \varphi \in C_c^\infty(\Omega; \mathbb{R}^d), \|\varphi(x)\| \leq 1 \forall x \in \Omega \right\}, \tag{1}$$

see for instance [2], and a function $u \in L^1(\Omega)$ is said to have bounded variation if and only if this quantity is finite. The space of such functions is usually denoted $BV(\Omega)$. Clearly, such a definition allows for discontinuous functions, as it is obvious that the characteristic function of a sufficiently regular set is a BV function.

*CMAP, Ecole Polytechnique, CNRS, 91128 Palaiseau, France.
email: antonin.chambolle@cmap.polytechnique.fr

†Institute for Computer Graphics and Vision, Graz University of Technology, 8010 Graz, Austria and Center for Vision, Automation & Control, AIT Austrian Institute of Technology GmbH, 1220 Vienna, Austria. email: pock@icg.tugraz.at

For this reason, it is not trivial to correctly discretize the functional $|Du|(\Omega)$. An obvious discretization, assuming to simplify $\Omega = [0,1]^2$, N is an integer, $h = 1/N > 0$ would be, given the discrete function $u^h = (u^h_{i,j})_{0 \leq i,j \leq N}$,

$$J_h(u^h) = \\ h \sum_{i<N, j<N} \sqrt{(u^h_{i+1,j} - u^h_{i,j})^2 + (u^h_{i,j+1} - u^h_{i,j})^2} + h \sum_{i=1}^{N-1} |u^h_{i+1,N} - u^h_{i,N}| + h \sum_{j=1}^{N-1} |u^h_{N,j+1} - u^h_{j,N}|. \tag{2}$$

The scaling h is the volume of the elementary "pixel" h^d (here $d = 2$) divided by the scale h which appears in the discrete gradients. Naively, this discretization appears to be wrong, as for instance the measure of a characteristic function ($u^h_{i,j} \in \{0,1\}$) will always be exaggerated, more or less strongly depending on the orientation of the boundary, see Fig. (1).

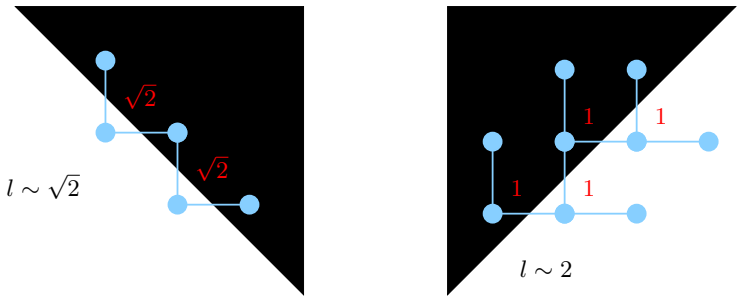

Figure 1: How J_h would measure a sharp slanted edge: on the left, we get the correct measure, on the right the result is biased by a factor $\sqrt{2}$, while a smoothed edge in the same direction can have a much lower energy. This explains why discrete minimizers of this approximation will have sharp edges in some orientation, and smoother edges in other.

However, this analysis is not really correct: as we are in practice interested in minimization problems involving J_h, the right question should be wether minimizers of such problems will approximate correctly the minimizer of some related continuous problem. This is expressed by the fact that J_h, as $h \to 0$, actually "Γ-converges" [10, 25] to $|Du|(\Omega)$ (the proof is more or less trivial, for instance see [13, 22] for examples of similar proofs for variants of J_h). But this result suffers from a slight drawback: since the measure of characteristic functions with J_h is wrong, it means that in this process, such a function in the limit will *not*, in general, be approximated by discrete characteristic functions. In practice, it is easy to see that it suffices to slightly smooth the limiting function u to obtain after discretization an image u^h with $J_h(u^h) \approx |Du|(\Omega)$. (Rigorous error estimates can be found for instance in [40, 34, 33], see also some references below for P1 finite elements error estimates.) This means that sharp discontinuities will exceptionally appear in minimizers of energies involving J_h (see [23] for many interesting examples).

This issue has been addressed many times in the imaging literature, in many contexts: finite differences [17, 20, 23], graph-based total variations [38, 9] (these references can by no means be exhaustive), more complex grids [32]... Others have advocated for finite elements discretizations [29, 30, 28], obtaining in particular very good results with adaptive meshes [3, 5, 4, 6, 7]. An obvious issue with $P1$ elements is the following: again, if one wants to approximate a discontinous function, then the gradient in some elements should be very large, and its orientation will be mostly determined by the directions of the edges of the element. This leads again to an exaggeration of the total variation of characteristic functions, and as a result, to a smoothing of the discrete variational solutions, unless adaption is (well) implemented.

In this paper, we discuss the merits of a finite elements discretization based on nonconforming P1 elements, also known as "Crouzeix-Raviart" finite elements since they were introduced in [24] (see also [11]). It has been observed many times that these can be useful to discretize some nonlinear variational problems such as Cavitation and Fracture [31, 41], Nonlinear Elasticity and Stokes's equation [27] (where it is extended to non-triangular meshes, which should also be interesting for total variation-based energies), Nonlinear Elasticity with mesh adaption [36, 35] — see [11] for a general overview of the use of this discretization over the years.

It turns out that these elements enjoy some very nice properties: in particular, the direction of the gradient in an element is entirely free and not determined by the shape of the element itself. This makes them particularly desirable to approximate functions with discontinuities, without altering the total measure of the singularity (see the quite elementary Prop 3.3 below). On the other hand, minimizers of a Crouzeix-Raviart-based total variation can be quite diffusive, for reasons different than the ones pointed out before, so that the need for adaptivity is not totally eliminated by this choice. We can propose, on square grids, a particular adaptive strategy which automatically derives the best way to cut elementary squares into two triangles in order to find the best approximation of a given image, from the point of view of diffusivity.

Throughout the paper we will mostly focus on the following "denoising" problem [39]:

$$\min_{u \in BV(\Omega)} |Du|(\Omega) + \frac{1}{2\tau} \int_\Omega (u - u^\diamond)^2 dx. \tag{3}$$

Here, $u^\diamond \in L^2(\Omega)$ is the original signal (in [39], a noisy image), u its regularized version, and $\tau > 0$ a parameter (which obviously controls the degree of smoothing).

The main reason for focusing on this problem is that its solution corresponds to evaluating the "proximity operator" of the total variation at $u^\diamond$, and can be used as a basic brick in many minimization algorithms involving the same functional (see [21] for an overview). Additionally, since we will focus mostly on the discretization of the first term in this problem, our study will apply with little or no change to many other second terms (and simple variants of the first).

The paper is organized as follows: in the next Section 2 we discuss the issues of approximating the gradient of BV functions and introduce the Crouzeix-Raviart finite elements, discussing their most useful properties in our context. Then, in Section 3, we define the Crouzeix-Raviart total variation and analyse some properties. We show in particular that straight lines (more precisely, step functions with straight jump) are measured perfectly by this energy, independently of the mesh. On the other hand, we can also build diffusive approximations to step functions. In

Section 4 we introduce a simple adaptive strategy, in 2D, to overcome this issue. We show numerical experiments, and comparison with other discretizations, in Section 5. Eventually, we propose in Section A a variant of our adaptive Crouzeix-Raviart discretization for 2D images, which has only one degree of freedom per pixel.

2 Crouzeix-Raviart approximation of BV functions

2.1 Discretization of the gradient of a BV function u

Consider $u \in BV(\Omega)$, $\Omega \subset \mathbb{R}^2$, a function with bounded variation and $\mathcal{T}^h = \{T_i : i = 1, \dots, N\}$ a triangular mesh of a polygonal approximation $\Omega^h \subset \Omega$ of Ω. Here $h > 0$, is the maximal size of an edge of a triangle T_i, $i = 1, \dots, N$, moreover one assumes $\operatorname{dist}(\Omega^h, \mathbb{R}^2 \setminus \Omega) \leq h$. Let for each triangle T_i,

$$\mathbf{p}_i := \frac{1}{|T_i|} \int_{T_i} Du. \tag{4}$$

Since Du is a measure, this is correctly defined provided $|Du|(\bigcup_{i=1}^N (\partial T_i)) = 0$, otherwise, one needs to arbitrarily assign the boundaries of the T_i to one of the adjacent triangles it belongs to: that is, for instance, replace T_1 with $\overline{T}_1$, T_2 with $\overline{T}_2 \setminus \overline{T}_1$, T_i with $\overline{T}_i \setminus \bigcup_{j<i} \overline{T}_j$ etc. Based on the vectors p_i, we define, for $x \in \Omega^h$ the piecewise constant function

$$\mathbf{p}^h(x) = \sum_i \mathbf{p}_i \chi_{T_i}(x), \tag{5}$$

where χ_{T_i} denotes the characteristic function of the triangle T_i. By construction, obviously,

$$\int_{\Omega^h} |\mathbf{p}^h(x)| dx \leq |Du|(\Omega^h) \leq |Du|(\Omega). \tag{6}$$

More precisely, if we introduce $\nu^h(x) = \mathbf{p}^h(x)/|\mathbf{p}^h(x)|$ (if $\mathbf{p}_i = 0$ for some triangle T_i, we can either choose arbitrarily $\nu^h(x)$ in T_i, or let $\nu^h(x) = 0$), we can derive the following error estimate:

Lemma 2.1. *Let $u \in BV(\Omega^h)$ be a function with bounded variation and let $p^h(x)$ be defined as in (5). Then,*

$$|Du|(\Omega^h) = \int_{\Omega^h} |\mathbf{p}^h(x)| dx + \frac{1}{2} \int_{\Omega^h} |\nu_u(x) - \nu^h(x)|^2 |Du|. \tag{7}$$

Proof. By direct calculation,

$$|Du|(\Omega^h) = \int_{\Omega^h} |Du| = \int_{\Omega^h} \nu_u(x) \cdot Du = \sum_{i=1}^N \int_{T_i} \nu^h(x) \cdot Du + \int_{\Omega^h} (\nu_u(x) - \nu^h(x)) \cdot Du$$

$$= \sum_{i=1}^N |\mathbf{p}_i||T_i| + \int_{\Omega^h} |Du| - \nu^h(x) \cdot \nu_u(x) |Du| = \int_{\Omega^h} |\mathbf{p}^h(x)| dx + \int_{\Omega^h} (1 - \nu^h(x) \cdot \nu_u(x)) |Du|$$

$$= \int_{\Omega^h} |\mathbf{p}^h(x)| dx + \frac{1}{2} \int_{\Omega^h} (|\nu_u(x)|^2 + |\nu^h(x)|^2 - 2\nu^h(x) \cdot \nu_u(x)) |Du|,$$

and the final estimate follows. □

The error estimate shows that the approximation will be better if the gradient direction $\nu_u = Du/|Du|$ does not oscillate too much in each triangle.

Remark 2.2. *Interestingly, it is easy to deduce that if $u = \chi_E$ is the characteristic function of a $C^{1,1}$ set E which satisfies both a R-inner and outer ball condition everywhere on ∂E (so that $|\kappa_E| \leq 1/R$, in particular), then if $h \leq R$,*

$$\left(1 - \frac{\pi^2}{18}\left(\frac{h}{R}\right)^2\right)|D\chi_E(\Omega^h)| \leq \int_{\Omega^h} |\mathbf{p}^h(x)|dx \leq |D\chi_E(\Omega^h)|. \tag{8}$$

Indeed, if $h \leq R$ then, thanks to the ball condition, for any triangle $T \in \mathcal{T}^h$, $\partial E \cap T$ is the intersection of T with a small piece of $C^{1,1}$ curve of length at most $\pi h/3$. Denoting by θ the angle of the normal vector of this curve with respect to e_1 and $\bar{\theta}$ the angle of ν^h, obviously $|\nu(x) - \nu^h| \leq |\theta(x) - \bar{\theta}|$. Observing that there must be a point on the piece of curve where $\nu^h = \nu(\bar{x})$ (as ν^h is in the cone generated by $\nu(x)$ for x on the curve), one has (using that θ is $(1/R)$-Lipschitz, and denoting dist *the distance along the curve)*

$$|\nu(x) - \nu^h| \leq |\theta(x) - \bar{\theta}| \leq \frac{1}{R}\mathrm{dist}\,(x, \bar{x}) \leq \frac{\pi h}{3R}.$$

Hence,

$$\int_T |\nu(x) - \nu^h|^2 |Du| \leq \frac{\pi^2 h^2}{9R^2}\mathcal{H}^1(\partial E \cap T)$$

and (8) *follows from* (7)*. (Under the very strong inner and outer ball conditions, this can be extended to any dimension, with a different constant.) A natural question is whether a similar estimate would hold, in 2D, for $u \in BV(\Omega)$ such that there exists $z \in L^\infty(\Omega; B(0,1))$ (or maybe continuous) with* $\mathrm{div}\, z \in L^\infty(\Omega)$ *and $z \cdot Du = |Du|$.*

2.2 Approximation of u

Now an important question is whether $\mathbf{p}^h$ can be considered as the discrete gradient of some discretized function u^h. It is in fact well known that it is the case, with the function u^h defined in a space of nonconforming finite elements interpolation called "Crouzeix-Raviart" finite elements [24, 11]. Although these are defined in any dimension, we restrict our analysis to the 2D case for simplicity (but we will mention explicitly when it cannot be extended easily to higher dimension).

We first claim that in a discrete sense, $\mathrm{curl}\,\mathbf{p}^h = 0$. The precise sense is (obviously) as follows: For any continuous and piecewise linear (P1) function $\varphi : \mathcal{T}^h \mapsto \mathbb{R}$ one has

$$\int_{\Omega^h} \mathbf{p}^h \cdot (\nabla\varphi)^\perp dx = 0, \tag{9}$$

where we denoted $(a,b)^\perp := (-b,a)$, for $(a,b) \in \mathbb{R}^2$ a counter-clock rotation by 90 degrees. Indeed, by definition, $\nabla\varphi$ is constant in each triangle T_i and will denote ist value by $(\nabla\varphi)_i$. Clearly, $\mathbf{p}^h$ is also constant on each triangle (with value $\mathbf{p}_i$), and therefore (9) becomes

$$\sum_{i=1}^N |T_i|\mathbf{p}_i \cdot (\nabla\varphi)_i^\perp = \sum_{i=1}^N \left(\int_{T_i} Du\right) \cdot (\nabla\varphi)_i^\perp = \int_\Omega (\nabla\varphi)^\perp \cdot Du = 0.$$

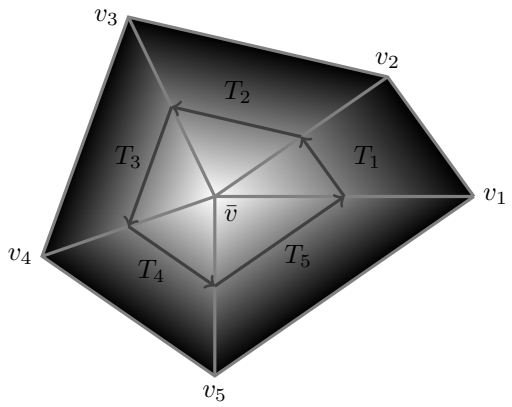

Figure 2: A set of ordered triangles T_i, $i = 1, ..., 5$ defined through the triplets $(v_i, v_{i+1}, \bar{v})$ with a common vertex $\bar{v}$ in the middle. In the background, we show the P1 function φ which is one at $\bar{v}$ and zero at the other vertices. In red we show the loop of vectors originating by the rotated and scaled gradients of the function ϕ passing through the middle of each edge.

as $\operatorname{curl} Du = 0$. To prove this rigorously, if $|Du|(\bigcup_{i=1}^N(\partial T_i)) = 0$ one can first approximate u with smooth functions, for which the integral is trivially zero, and pass to the limit, if not, one can first approximate the mesh and φ with a slightly perturbed mesh $\mathcal{T}' = \{T_i' : i = 1, \dots, N\}$ and φ' such that $|Du|(\bigcup_{i=1}^N(\partial T_i')) = 0$ and $\int_\Omega(\nabla\varphi')^\perp \cdot Du \approx \int_\Omega(\nabla\varphi)^\perp \cdot Du = 0$ and pass to the limit.

Let us now show that one can integrate back any discrete field $\mathbf{p}^h$ satisfying (9) into a function u^h, which is, if $\mathbf{p}^h$ was obtained from (4), an approximation of u. In Figure 2 we consider a vertex $\bar{v}$ which is common to a set of ordered triangles T_i, $i = 1, ..., N$ of a triangulation $\mathcal{T}^h$, defined via the triplets $(v_i, v_{i+1}, \bar{v})$ and $v_{N+1} = v_1$ Moreover, we consider for φ in (9) a function equal to 1 in the vertex $\bar{v}$ and zero in all other vertices $v_1, ..., v_{N+1}$. The rotated gradients $(\nabla\varphi)_i^\perp$ in the triangles are given by

$$(\nabla\varphi)_i^\perp = \frac{v_{i+1} - v_i}{h_i|v_{i+1} - v_i|} = \frac{v_{i+1} - v_i}{|T_i|},$$

where h_i denotes the height of the triangle relative to the edge (v_i, v_{i+1}). Then, (9) becomes

$$\int_{\Omega^h} \mathbf{p}^h \cdot (\nabla\varphi)^\perp dx = \sum_{i=1}^N |T_i|\mathbf{p}_i \cdot (\nabla\varphi)_i^\perp = \sum_{i=1}^N \mathbf{p}_i \cdot (v_{i+1} - v_i) = 0$$

that is, the circulation of $\mathbf{p}^h$ around the loop $v_1, ..., v_{N+1}$ vanishes. In particular, the circulation of $\mathbf{p}^h$ also vanishes for all loops passing the points $\alpha v_i + (1 - \alpha)\bar{v}$ for $\alpha \in [0, 1]$. The most interesting case is $\alpha = \frac{1}{2}$ since it yields points in the middle of the edges which are also part of neighboring loops. It follows that one can assign a (unique up to a global constant) values u_e in the middle of each edge e of the whole triangulation (at least if the domain is simply connected). We will soon see a more global characterization of $\mathbf{p}^h$ which allows to consider it as a discrete gradient in arbitrary domains (and dimension), see Lemma 2.3.

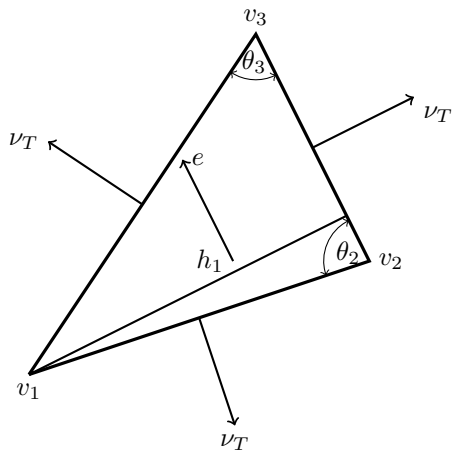

Figure 3: A triangle $T = (v_1, v_2, v_3) \in \mathcal{T}^h$ together with its outer normals ν_T, the normalized edge direction $e = (v_3 - v_2)/|v_3 - v_2|$ shown and the two angles $\theta_3 = \widehat{v_1 v_3 v_2}$ and $\theta_2 = \widehat{v_3 v_2 v_1}$.

Actually, if $\mathbf{p}^h$ is obtained through (4), one checks easily that in addition, the correct value to assign in the middle of an edge is the average of u on the edge. Indeed, Figure 3 shows a triangle $T = (v_1, v_2, v_3) \in \mathcal{T}^h$, where we have chose the normalized edge direction $e = (v_3 - v_2)/|v_3 - v_2|$. Then, one has (assuming $|Du|(\partial T) = 0$, otherwise one would need to first do the computation on a slightly translated triangle and then pass to the limit)

$$\int_T e \cdot Du = \int_{\partial T} u(x) e \cdot \nu_T d\mathcal{H}^1 = \sin(\theta_3) \int_{[v_1,v_3]} u dx - \sin(\theta_2) \int_{[v_1,v_2]} u dx.$$

Denoting h_1 the height from v_1, one has $h_1 = |v_2 - v_1| \sin(\theta_2) = |v_3 - v_1| \sin(\theta_3)$ and $|T| = h_1 |v_3 - v_2|/2$, so that we have

$$\mathbf{p}^h \cdot e = \frac{1}{|T|} \int_T e \cdot Du = \frac{2}{|v_3 - v_2|} \left(\fint_{[v_1,v_3]} u dx - \fint_{[v_1,v_2]} u dx \right).$$

The right-hand side is exactly the gradient, in the direction e, of the affine function which is equal in the middle of each edge $[v_i, v_j]$ to $\fint_{[v_i,v_j]} u dx$.

In the next section, we consider a better characterization of Crouzeix-Raviart gradients (which is also easier to handle in arbitrary dimension).

2.3 Characterization of Crouzeix-Raviart gradients

We introduce, given the mesh $\mathcal{T}^h$, the set $\mathcal{N}(\mathcal{T}^h)$ of nodes which are the middle points of the edges of the triangles of $\mathcal{T}^h$. Moreover, we define the nonconforming Crouzeix-Raviart (CR) finite-element space

$$V(\mathcal{T}^h) = \left\{ u : \Omega^h \to \mathbb{R} \,:\, u_{|T} \text{ affine } \forall T \in \mathcal{T}^h,\ u \text{ continuous at } x,\ \forall x \in \mathcal{N}(\mathcal{T}^h) \right\}.$$

In this space, the gradient $\mathbf{p}^h = D_h u$ of a function u is defined as the vectorial function which coincides with $\nabla u_{|T}$ on each triangle (and we will denote $D_h u(T)$ its value in the triangle T). We call it a "Crouzeix-Raviart (CR) gradient", and observe that this field is a P0 finite elements vector field, that is, a vector field which is constant on each triangle. The analysis in the previous section shows that for any $u \in BV(\Omega)$ with $|Du|(\bigcup_{i=1}^N \partial T_i) = 0$, the function u^h defined by assigning to $x \in \mathcal{N}(\mathcal{T}^h)$ the average value of u on the edge through x, and affine with slope $\mathbf{p}_i$, given by (4), in each T_i, belongs to $V(\mathcal{T}^h)$. (We call it the projection of u to $V(\mathcal{T}^h)$, and it is naturally extended to any $u \in BV(\Omega)$ by assigning the boundaries $\bigcup_{i=1}^N \partial T_i$ arbitrarily to one of the neighbouring triangle, such as the one with lower index as already suggested). In particular, $\mathbf{p}^h$, given by (5), is a CR gradient.

In the following, we give a characterization of CR gradients which is more precise than (9). It is based on zeroth order "Raviart Thomas" (RT0) vector fields [37], which are defined by their fluxes across the edges of the triangulation. Inside the triangles, RT0 fields are affine functions and they are continuous across the edges of the mesh. Given a triangle $T = (v_1, v_2, v_3)$, the RT0 field $\phi_T(x)$ inside the triangle T is given by

$$\phi_T(x) = \frac{f_1}{h_1|v_3 - v_2|}(x - v_1) + \frac{f_2}{h_2|v_3 - v_1|}(x - v_2) + \frac{f_3}{h_3|v_2 - v_1|}(x - v_3),$$

where f_i are the fluxes through the edges e_i which are opposite to the vertex v_i and h_i are the heights relative to the vertex v_i. With this choice the flux of the field $\phi_T(x)$ through each edge e_i with outward normal ν_i is constant. Indeed, for $x \in e_1 = [v_2, v_3]$,

$$\phi_T(x) \cdot \nu_1 = \frac{f_1(x - v_1) \cdot \nu_1}{h_1|v_3 - v_2|} + \frac{f_2(x - v_2) \cdot \nu_1}{h_2|v_3 - v_1|} + \frac{f_3(x - v_3) \cdot \nu_1}{h_3|v_2 - v_1|} = \frac{f_1}{|v_3 - v_2|}$$

since $(x - v_1) \cdot \nu_1 = h_1$ and $(x - v_2) \cdot \nu_1 = (x - v_3) \cdot \nu_1 = 0$. Hence

$$\int_{e_1} \phi_T(x) \cdot \nu_1 d\mathcal{H}^1 = f_1,$$

and the total flux through the edges of T is given by (denoting $\nu_T \in \{\nu_1, \nu_2, \nu_3\}$ the outwards normal to T):

$$\int_{\partial T} \phi_T \cdot \nu_T d\mathcal{H}^1 = f_1 + f_2 + f_3.$$

The following result establishes a relationship between CR gradients and zero-divergence RT0 fields.

Lemma 2.3. *The P0 field $\mathbf{p}^h$ is a CR gradient if and only if it is orthogonal to all zero-divergence RT0 fields ϕ with vanishing fluxes on $\partial\Omega^h$, that is*

$$\int_{\Omega^h} \phi \cdot \mathbf{p}^h \, dx = 0.$$

Proof. First, we show that CR gradients are orthogonal to zero divergence RT0 fields. Given a RT0 field ϕ defined in Ω^h and $u^h \in V(\mathcal{T}^h)$ with $\mathbf{p}^h = D_h u^h$ (which can be the projection, as mentioned, of a BV function u), then for $T_i \in \mathcal{T}^h$,

$$\int_{T_i} \phi \cdot \mathbf{p}^h \, dx = \int_{\partial T_i} u^h \phi \cdot \nu_{T_i} d\mathcal{H}^1 - \int_{T_i} u^h \mathrm{div}\, \mathbf{p}^h dx,$$

where in the second integral, u^h is the inner trace of the affine function u^h in the triangle (recall that this function may be discontinuous through the edges of the triangle). Since $\phi \cdot \nu_{T_i}$ is constant on each edge $(e^i_j)_{j=1,2,3}$ of T_i, and since u^h has, on e^i_j, average value $u^h(x^i_j)$ where $x^i_j \in \mathcal{N}(\mathcal{T}^h)$ is the middle point of e^i_j, it yields

$$\int_{T_i} \phi \cdot \mathbf{p}^h \, dx = \sum_{j=1}^{3} |e^i_j| u^h(x^i_j) \phi \cdot \nu^i_j - \int_{T_i} u^h \mathrm{div}\, \mathbf{p}^h dx.$$

If $T_{i'}$ is a neighbouring triangle and $e^{i'}_{j'} = e^i_j$ the common edge, as u^h is continuous at $x^i_j = x^{i'}_{j'}$ and $\nu^i_j = -\nu^{i'}_{j'}$,

$$|e^i_j| u^h(x^i_j) \phi \cdot \nu^i_j + |e^{i'}_{j'}| u^h(x^{i'}_{j'}) \phi \cdot \nu^{i'}_{j'} = 0.$$

Hence summing on all triangles, we obtain the general Green formula:

$$\int_{\Omega^h} \phi \cdot D_h u^h \, dx = \int_{\partial \Omega^h} u^h \phi \cdot \nu_{\Omega^h} d\mathcal{H}^1 - \int_{\Omega^h} u^h \mathrm{div}\, \phi \, dx. \tag{10}$$

(Remark that if u^h was obtained as the projection of a BV function u, then the second integral is also $\int_{\partial \Omega^h} u \phi \cdot \nu_{\Omega^h} d\mathcal{H}^1$.) In particular, if $\mathrm{div}\, \phi = 0$ and ϕ vanishes on $\partial \Omega^h$, we find

$$\int_{\Omega^h} \phi \cdot \mathbf{p}^h \, dx = 0.$$

Now, we show that if $\mathbf{p}^h$ is orthogonal to a zero-divergence RT0 field, then it is a CR gradient. Assume we are given a 2D $P0$ vector field $\mathbf{p}^h$ such that $\int_{\Omega^h} \phi \cdot \mathbf{p}^h dx = 0$ for all divergence free RT0 vector fields ϕ with vanishing fluxes on the boundary of Ω^h. Let $x^0, x^1 \in \mathcal{N}(\mathcal{T}^h)$ be two midpoints of edges of the triangulation and assume we are given two different piecewise linear simple paths from x^0 to x^1, intersecting at most once each triangle by joining two nodes of $\mathcal{N}(\mathcal{T}^h)$ by a straight segment. Letting $u(x^0) = 0$, we can integrate $\mathbf{p}^h$ along each path Γ^i, $i = 1, 2$, to obtain two different values $u^i(x^1)$, $i = 1, 2$. If these values are the same (i.e. independent on the path), the circulation of $\mathbf{p}^h$ along the path Γ^1 followed by Γ^2 will be zero, which in turn implies that $\mathbf{p}^h$ is a CR gradient.

Indeed, we can identify each path with a Raviart-Thomas vector field ϕ^i, such that the flux through an edge is 1 when the path crosses the edge, moving forward. Then, $\phi = \phi^2 - \phi^1$ is divergence free so that

$$\int \mathbf{p}^h \cdot \phi^1 dx = \int \mathbf{p}^h \cdot \phi^2 dx.$$

The same computation as before shows that this is equivalent to $u^1(x^1) = u^2(x^1)$. □

2.4 Further obvious remarks

Given $u \in V(\mathcal{T}^h)$, we may define a P0 function u_0 by averaging u in each triangle $T \in \mathcal{T}^h$. Obviously (as u is affine in T), the value thus obtained is the same as the value in the center (of mass) c_T of the triangle, and the average of the three mid-point values of the edges. One has

$$\int_T |u(x) - u(c_T)| dx \leq |D_h u(T)| \int_T |x - c_T| dx \leq h|T||D_h u(T)|.$$

In particular, summing on all triangles we find that:

$$\|u - u_0\|_{L^1(\Omega^h)} \leq h \int_{\Omega^h} |D_h u| dx. \tag{11}$$

The same would also clearly hold with a L^p norm on both sides, replacing the L^1 norm, for $p \in [1, \infty]$. See for instance [12] for more general estimates.

3 Definition of a Crouzeix-Raviart discrete total variation

3.1 Definition, and approximation properties

Given then $u \in V(\mathcal{T}^h)$, we define the approximate total variation

$$J_h(u) := \int_{\Omega^h} |D_h u| dx = \sum_{T \in \mathcal{T}^h} |T| |D_h u(T)|. \tag{12}$$

Here we recall that $D_h u(T)$ is the gradient of u in each triangle T (and not across the edges of the triangles). In this section, we show that in a variational sense, J_h is an approximation of the total variation.

The following result is obvious, considering the analysis in the previous sections. We assume that we are given an arbitrary family of triangulations $\mathcal{T}^h$, with $h \to 0$.

Proposition 3.1. *J_h Γ-converges to the total variation (1) as $h \to 0$, in $L^1(\Omega)$, as well as for the distributional convergence.*

Although the latter convergence is quite weak, we will see later on that without further assumption on the triangulations we can hardly hope for compactness in a better sense.

Proof. As we have seen, for any $u \in L^1(\Omega)$ with finite total variation, one can build u^h which will go to u as $h \to 0$, and such that $J_h(u^h) \to |Du|(\Omega)$. Conversely, if u^h is a sequence which converges to some u and $\sup_h J_h(u^h) < +\infty$, then clearly $\mathbf{p}^h(x)$ is bounded as a measure and converges weakly-$*$ (up to subsequences) to some measure $\mathbf{p} \in \mathcal{M}(\Omega; \mathbb{R}^2)$. The fact that $\mathbf{p}$ is orthogonal to zero divergence fields is is easy to show by approximating compactly supported smooth vanishing divergence fields with RT0 fields and using Lemma 2.3. Moreover one obviously have

$$\int_\Omega |\mathbf{p}| \leq \liminf_{h \to 0} J_h(u^h).$$

It remains therefore to show that $\mathbf{p} = Du$. This will follow from the compactness result which we now state in Proprosition 3.2. □

Proposition 3.2. *Let $u^h \in V(\mathcal{T}^h)$ such that $\sup_h J(u^h) < +\infty$. Then, there exists a subsequence (u^{h_k}) and a constant $c_{h_k} \in \mathbb{R}$, and $u \in BV(\Omega)$, such that $u^{h_k} - c_{h_k} \to u$ in the sense of distributions in Ω as $k \to \infty$ (and $|Du|(\Omega) \leq \liminf_k J_{h_k}(u^{h_k})$).*

Moreover, if we assume that the triangulations are uniformly regular (in the classical sense: there exists $\bar{\theta} > 0$ such that the angles of the triangles are all larger than $\bar{\theta}$, or equivalently,

there exists $\delta > 0$ such that for any triangle $T = (v_1, v_2, v_3) \in \mathcal{T}^h$, $h_3 \geq \delta |v_3 - v_1|$ where $h_3 = \mathrm{dist}\,(v_3, (v_1, v_2))$ is the height of T from v_3), then the convergence $u^{h_k} - c_{h_k} \to u$ is strong in $L^p(\Omega)$ for any $p < 2$, and weak in $L^2(\Omega)$.

Proof. As we have seen, up to a subsequence, $\mathbf{p}^{h_k} := D_{h_k} u^{h_k} \overset{*}{\rightharpoonup} \mathbf{p}$ as measures and $\mathbf{p} = Du$ for some function $u \in BV(\Omega)$. We need to show that u is the limit of the u^{h_k} (up to constants).

First, without further assumption on the triangulations, the following is true: given ϕ a C^1, compactly supported field and ϕ^h the RT0 fields obtained by evaluating the fluxes of ϕ across the edges of $\mathcal{T}^h$, one still has thanks to (10):

$$\int_{\Omega^{h_k}} u^{h_k} \mathrm{div}\, \phi^{h_k} dx = -\int_{\Omega^{h_k}} \phi^{h_k} \cdot D_{h_k} u^{h_k} dx \to -\int_\Omega \phi \cdot Du = \int_\Omega u \,\mathrm{div}\, \phi dx$$

as $k \to \infty$. The first integral, on the other hand (using the notation of Section 2.4) is also

$$\sum_{T \subset \Omega} \int_T u^{h_k}(x) dx \frac{1}{|T|} \int_T \mathrm{div}\, \phi(y) dy = \sum_{T \subset \Omega} u_0^{h_k}(T) \int_T \mathrm{div}\, \phi(y) dy = \int_{\Omega^h} u_0^{h_k} \mathrm{div}\, \phi(y) dy$$

so that we conclude that $u_0^{h_k} \to u$ (up to constants, one should for instance remove the averages of all the functions) in the distributional sense (and u^{h_k} as well, thanks to (11)).

We now assume in addition that the triangulations are uniformly regular, and consider again the P0 functions u_0^h. Observe that the jump of u_0^h across an edge $[v_2, v_3]$ common to two triangles $T = (v_1, v_2, v_3)$ and $T' = (v_2, v_3, v_4)$ is given by $D_h u^h(T) \cdot (2v_1 - v_2 - v_3)/6 - D_h u^h(T') \cdot (2v_4 - v_2 - v_3)/6$ (we recall that $u_0^h(T)$ is both given by the average of u^h in T triangle and by the middle value $u^h((v_1 + v_2 + v_3)/3)$). Hence,

$$|u_0^h(T) - u_0^h(T')||v_3 - v_2| \leq |D_h u^h(T)| \frac{|v_3 - v_2||2v_1 - v_2 - v_3|}{6} + |D_h u^h(T')| \frac{|v_3 - v_2||2v_4 - v_2 - v_3|}{6}.$$

By the regularity assumption, $|v_3 - v_2||2v_1 - v_2 - v_3| \leq |v_3 - v_2||v_1 - v_2| + |v_3 - v_2||v_1 - v_3| \leq 2|T|/\delta$, hence

$$|u_0^h(T) - u_0^h(T')||v_3 - v_2| \leq \frac{1}{3\delta} \left(|T||D_h u^h(T)| + |T'||D_h u^h(T')| \right).$$

Summing on all the edges, it follows that (seing the P0 function u_0^h as a piecewise constant function with bounded variation)

$$\int_{\Omega^h} |D u_0^h| \leq \frac{1}{\delta} J_h(u^h).$$

Hence, up to a constant, u_0^h is bounded in $L^2(\Omega)$ and compact in $L^p(\Omega)$, $p < 2$. We conclude thanks to (11). We could have used general estimates for nonconforming finite elements, such as found in [12, Chap. 10]. □

3.2 The measure of straight lines

The Green formula (10) shows that J_h satisfies the following lower estimate, for $u \in V(\mathcal{T}^h)$ and ϕ^h a RT0 field:

$$J_h(u) \geq \sup \left\{ \int_{\partial \Omega^h} u \phi^h \cdot \nu_{\Omega^h} d\mathcal{H}^1 - \int_{\Omega^h} u \mathrm{div}\, \phi^h dx : |\phi^h(c_T)| \leq 1 \, \forall T \in \mathcal{T}^h \right\}, \tag{13}$$

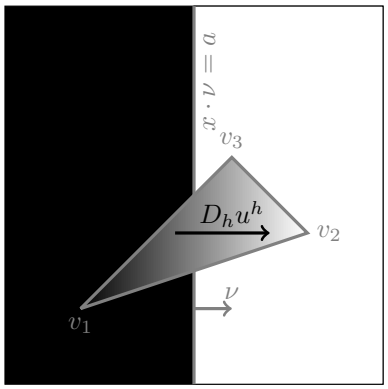

Figure 4: The figure shows the function u^h and its gradient for one triangle $T = (v_1, v_2, v_3)$ approximating the characteristic function of the half space $x \cdot \nu > a$ with $\nu = (1, 0)$ and $a \in \mathbb{R}$. The function u^h inside the triangle is affine with a gradient $D_h u^h$ which is simply a mutiple of the normal ν.

where we recall that c_T refers to the center of the respective triangle T.

This formula would be an interesting way to build lower estimates for variational problems involving J_h if it were easy to build test RT0 fields ϕ^h satisfying the constraint, possibly from fields in the continuum. However, it is easy to check that given $\phi \in C_c^\infty(\Omega; \mathbb{R}^2)$ with $|\phi| \leq 1$ everywhere, the RT0 projection ϕ^h defined by assigning on each edge of the triangulation the flux of ϕ through the edge needs not satisfy $|\phi^h(c_T)| \leq 1$ (and can be substantially larger, independently on the mesh size h).

There is however one trivial situation where this can be used, and we obtain the following result, valid for any triangulation $\mathcal{T}^h$ of Ω:

Proposition 3.3. *Let $\nu \in \mathbb{S}^1$ be a unit vector, $a \in \mathbb{R}$ and $u = \chi_{\{x \cdot \nu > a\}}$. Let u^h be the projection of u on CR functions, obtained by letting $D_h u^h(T) = \nu \mathcal{H}^1(\{x \cdot \nu = a\} \cap T)/|T|$ in each triangle $T \in \mathcal{T}^h$. Then for any CR function v with $v = u^h$ on $\mathcal{N}(\mathcal{T}^h) \cap \partial\Omega^h$,*

$$J_h(v) \geq J_h(u^h) = \mathcal{H}^1(\{x \cdot \nu = a\} \cap \Omega^h).$$

The proposition shows (see also Figure 4) that in some sense, the discrete functional J_h is perfectly isotropic, as its minimal value for a straight edge coincides with the length of the edge whatever the direction ν. We will see soon that unfortunately, this is not enough to make J_h a "perfect" approximation of the total variation.

Proof. The fact that $J_h(u^h) = \mathcal{H}^1(\{x \cdot \nu = a\} \cap \Omega^h)$ follows from (7). The other inequality follows from (13). Indeed, consider the constant field ν, which is of course a particular RT0 field defined on $\mathcal{T}^h$ with norm less or equal to 1. We have therefore:

$$J_h(v) \geq \int_{\Omega^h} \nu \cdot D_h v = \int_{\Omega^h} \nu \cdot D_h u^h + \int_{\Omega^h} \nu \cdot D_h(v - u^h) = J_h(u^h) + \int_{\Omega^h} \nu \cdot D_h(v - u^h).$$

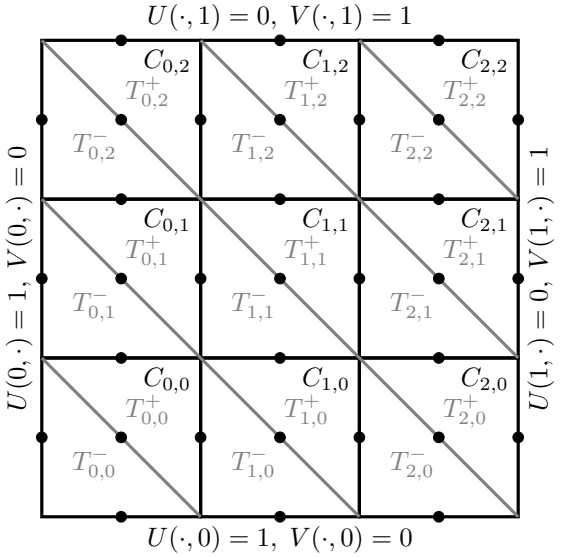

Figure 5: Discretization of the unit square $\Omega^h = [0,1]^2$, $h = 1/3$ using squares $C_{0,0}, ..., C_{2,2}$ each of size h^2. Each square $C_{i,j}$ is then divided into an upper triangle $T^+_{i,j}$ and a lower triangle $T^-_{i,j}$. The nodes of the mesh, represented as black dots, are in the middle of the edges of the triangles. Note the boundary conditions imposed by the functions $U(x,y)$ and $V(x,y)$.

Now, thanks to (10),

$$\int_{\Omega^h} \nu \cdot D_h(v - u^h) = \int_{\partial\Omega^h} (v - u^h)\nu \cdot \nu_{\Omega^h}$$

and this vanishes since we have assumed that $v = u^h$ on all the midpoints of the edges of the triangles which form $\partial\Omega^h$. □

3.3 The bad news

Proposition 3.3 shows that in theory, J_h is an excellent approximation of the total variation, which does not suffer from metrication errors or anisotropy as most other, in both the finite differences (such as graph based TVs [8], "isotropic" ℓ_2-TV [16]) or finite elements (P1 based [3]) settings. However, we will show that it does not mean that the corresponding solution is always sharp: we now show a particular example where in addition to the projection u^h (which is sharp), we can build infinitely many other solutions with the same energy (and a transition width which of course will go to zero as $h \to 0$), for which the transition occurs across a large number of elements.

The setting is as follows: $\Omega = \Omega^h = [0,1]^2$, $h = 1/n$, $n \geq 1$ divided in squares $C_{i,j} = [(ih, jh), ((i+1)h, jh)) \times [(ih, jh), (ih, (j+1)h))$ for $i = 0, \ldots, n-1$, $j = 0, \ldots, n-1$. Then, each square $C_{i,j}$ is divided into two triangles $T^{\pm}_{i,j}$ with $T^-_{i,j} = C_{i,j} \cap \{x + y \leq (i+j+1)h\}$ and $T^+_{i,j} = C_{i,j} \cap \{x + y > (i+j+1)h\}$, see Figure 5. We recall that the nodes $\mathcal{N}(\{T^{\pm}_{i,j}\})$ of

the mesh are the middle of the edges of the triangles, hence, here, the points $((i+1/2)h, jh)$, $(ih, (j+1/2)h)$, and $((i+1/2)h, (j+1/2)h)$.

Consider now the boundary conditions $U(x,y) = 1$ if $x = 0$ or $y = 0$, $U(x,y) = 0$ if $x = 1$ or $y = 1$, and $V(x,y) = 1$ if $x = 0$ or $y = 1$, and $V(x,y) = 0$ if $x = 1$ or $y = 0$. Clearly, Proposition 3.3 shows that the problems

$$\min_{u=U \text{ on } \partial\Omega\cap\mathcal{N}(\{T^{\pm}_{i,j}\})} J_h(u) \quad \text{and} \quad \min_{v=V \text{ on } \partial\Omega\cap\mathcal{N}(\{T^{\pm}_{i,j}\})} J_h(v) \tag{14}$$

where the minimizers are taken on CR functions on the mesh $\{T^{\pm}_{i,j}\}$, have both value $\sqrt{2}$. Moreover, a solution is given, for the first, by $u = \chi_{\{x+y\leq 1\}}$ (that is, the exact solution) on all nodes with $i + j \neq n$, and $u \in [0,1]$ in any node with $i + j = n$. For the second we can find a solution considering the projection of $\chi_{\{x\leq y\}}$ on the CR functions: that is, the functions v with $v(x,y) = 1$ on all nodes with $x < y$, $v(x,y) = 0$ on all nodes with $x > y$, and $v(x,y) = 1/2$ on the nodes with $x = y$. We claim that if there are infinitely many solutions to the first problem in (14), they are all concentrated (their gradient is not zero only near the axis $x + y = 1$) and may differ from u only near the line $\{x + y = 1\}$. On the other hand, there are also infinitely many solutions to the second, but now they can be very diffusive, and in particular solutions v' with $0 < v' < 1$ on all the interior nodes.

To prove the first claim, we observe that for any solution u and for all i, u has to go from 1 to 0 along the "vertical" chain of vertices $((i+1/2)h, j)$, $j = 0, \dots, n$. It follows that $\int_\Omega (D_h u)_1 dx = -1$. Similarly, $\int_\Omega (D_h u)_2 dx = -1$. Hence,

$$2 = -\int_\Omega (D_h u)_1 + (D_h u)_2 dx \leq \sqrt{2} \int_\Omega |D_h u| dx$$

using the 2D Cauchy-Schwartz inequality, pointwise. Since the right-hand side of this expression is also 2, it means that these inequalities are in fact equalities, and in particular that for a.e. x, $(D_h u)_1(x) = (D_h u)_2(x)$. As a consequence, in each triangle $T^{\pm}_{i,j}$, the values of u at the middle of the two shorter edges are equal. Using the boundary condition, it follows that u is unique except possibly on the middle vertices with $x + y = 1$ and thus in the triangles which contain them. It is easy to see that one can assign any arbitrary value $u(ih + h/2, (n-i)h - h/2) \in [0,1]$. at each of these nodes without changing the value of the energy.

We now focus on the second claim. Observe that if v is a minimizer of the second problem in (14), one must have now, for the same reasons as for u,

$$2 = \int_\Omega (D_h v)_1 - (D_h v)_2 dx \leq \sqrt{2} \int_\Omega |D_h v| dx = 2$$

so that $(D_h v)_1 = -(D_h v)_2 \geq 0$ a.e.

But now, this just imposes that the value of v in the middle of the longer edge of each triangle is the average of the two values in the middle of the shorter edges. Moreover, any CR function v which satisfies this condition and is globally nondecreasing from 0 to 1 along the nodes in the direction $(-1, 1)$ has minimal energy (as it will satisfy equality in the above equation).

Let us build a solution v "as diffusive as possible" (we would like to make this claim rigorous, however it is not clear how).

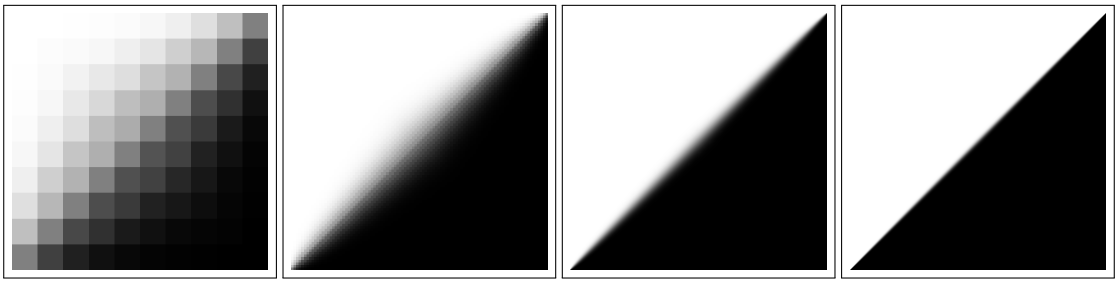

(a) $n = 10$ (b) $n = 100$ (c) $n = 1000$ (d) $n = 10000$

Figure 6: The smooth transition for different numbers of n, where we only plot the values $v_{i+1/2,j+1/2}$. Observe that only for a very fine mesh ($n = 10000$) we obtain a reasonably sharp transition.

To simplify: we will look for solutions which satisfy the symmetry, for all $(x, y) \in (0, 1)^2$,

$$v(x, y) + v(y, x) = 1.$$

In fact, if v is an arbitrary solution, then so is $(x, y) \mapsto 1 - v(y, x)$, hence so is also $1/2 + (v(x, y) - v(y, x))/2$ which has the above symmetry and essentially a larger transition than v. Hence assuming this symmetry is not too restrictive when looking for diffuse solutions. Similarly, we will assume that v is symmetric with respect to the axis $\{x+y = 1\}$: $v(x, y) = v(1-y, 1-x)$.

In particular, we have that $v'(x, x) = 1/2$, and $v'(x, y) \leq 1/2$ if $x \geq y$. We build a v in $\{y \leq x \leq 1 - y\}$. We claim (and this is all we know for sure) that this is the solution with the largest values $v_{i-1,1/2}, v_{i,1/2}$, $1 \leq i \leq n$.

The first observation is that if $v_{1/2,1/2} = 1/2$, then the largest possible value for $v_{1,1/2}$ is also $1/2$. But then, since $v_{3/2,0} = 0$, one has $v_{3/2,1/2} = 1/4$. Then the largest possible value $v_{2,1/2}$ is also $1/4$, etc. One finds that the largest possible value of v in the first line is by taking $v_{(i-1/2),1/2} = v_{i,1/2} = 1/2^{i+1}$.

We build then v by assuming that it is constant on the triangles $T^+_{i,j}$, at least as long as $i + j < n$. It will be clear later on why a "bad" v has to have such an oscillating gradient. One has

- $v_{i+1/2,i+1/2} = 1/2$ for $i \geq 0$;
- $v_{i+1/2,0} = 0$ for $i \geq 0$;
- $v_{i+1/2,j+1/2} = v_{i+1,j+1/2} = v_{i+1/2,j+1}$ for $i \geq j \geq 0$, $i + j \leq n - 1$;
- $v_{i+1/2,j+1/2} = (v_{i,j+1/2} + v_{i+1/2,j})/2$.

In particular, we deduce that

$$v_{i+1/2,j+1/2} = \frac{v_{i-1/2,j+1/2} + v_{i+1/2,j-1/2}}{2}.$$

Now, we introduce the variables $\xi_{i-j}^{i+j} = v_{i+1/2,j+1/2}$. One has $\xi_0^{2i} = 1/2$ for $i \geq 0$, and

$$\xi_l^m = \frac{\xi_{l-1}^{m-1} + \xi_{l+1}^{m-1}}{2} = \frac{1}{4}\xi_{l-2}^{m-2} + \frac{1}{2}\xi_l^{m-2} + \frac{1}{4}\xi_{l+2}^{m-2}.$$

For m even and $l = 2$, this reduces to

$$\xi_2^m = \frac{1}{8} + \frac{1}{2}\xi_2^{m-2} + \frac{1}{4}\xi_3^{m-2}.$$

Denoting now, $\zeta_l^m = \xi_{2l}^{2m}$, $l \geq 1$, we find that ($\zeta_l^0 = 0$ and) for $m \geq 1$,

$$\zeta^m = \frac{1}{4}\begin{pmatrix} 2 & 1 & 0 & 0 & \dots \\ 1 & 2 & 1 & 0 & \ddots \\ 0 & 1 & 2 & 1 & \ddots \\ \vdots & \ddots & \ddots & \ddots & \ddots \end{pmatrix} \zeta^{m-1} + \begin{pmatrix} \frac{1}{8} \\ 0 \\ 0 \\ \vdots \end{pmatrix}$$

Denoting B the matrix appearing in the recursion, we find that we must choose

$$\zeta^m = \left(\sum_{l=0}^{m-1} B^l\right)\begin{pmatrix} \frac{1}{8} \\ 0 \\ \vdots \end{pmatrix} = (I-B)^{-1}(I-B^m)\begin{pmatrix} \frac{1}{8} \\ 0 \\ \vdots \end{pmatrix}. \tag{15}$$

From there, we can go back to build v in $\{y < x < 1-y\}$, and then by symmetry in the whole square $[0,1]^2$. This shows that one can find a solution v, in that case, with a quite large transition layer. Of course any convex combination between this function and the function which is $1/2$ only at nodes where $x = y$, and equal to $\chi_{\{y>x\}}$ elsewhere, provides another solution.

In (15), we did not specify the size of the matrices: in fact, it is enough to take these of size larger than $n/2$ to compute v in a mesh of size $n \times n$. Choosing therefore $M > n/2$ we consider the $M \times M$ matrix

$$\frac{1}{4}\begin{pmatrix} 2 & 1 & 0 & 0 & \dots \\ 1 & 2 & 1 & 0 & \ddots \\ 0 & 1 & 2 & 1 & \ddots \\ \vdots & \ddots & \ddots & \ddots & \ddots \\ 0 & \dots & 0 & 1 & 2 \end{pmatrix}$$

This matrix has the M eigenvectors $e_k = (\sin(lk\pi/(M+1)))_{l=1}^M$, for $k = 1, \dots, M$, corresponding to the eigenvalues, respectively, $(1 + \cos(k\pi/(M+1)))/2 = \cos^2(k\pi/(2(M+1)))$. One can therefore compute (at least numerically) solutions ζ^m for large values of m, using that

$$\langle \zeta^m, e_k \rangle = \frac{1 - \cos^{2m}(k\pi/(2(M+1)))}{4\sin(k\pi/(2(M+1)))}\cos(k\pi/(2(M+1))) \tag{16}$$

and $\zeta^m = \sum_k \langle \zeta^m, e_k \rangle e_k / \|e_k\|^2$. We show in Fig. 6 a plot of the corresponding function v for various n.

4 Implementation with adaptive meshes

In this section we propose, for a quadrangular mesh in 2D, an adaptive CR finite elements discretization which is based on the important observation that the triangulation $(T_{i,j}^{\pm})$ shares the same nodes as the triangulation obtained by dividing each $C_{i,j}$ in the other possible way, that is, along the axis $\{x - ih = y - jh\}$.

Let us define v' as the function which is equal to v (defined in the previous section) on the nodes, but is now a CR function on the flipped mesh. Then, in all the squares $C_{i,j}$ where v was constant in one of the triangles $T_{i,j}^{\pm}$ ($T_{i,j}^{+}$ for $i+j<n$, $T_{i,j}^{-}$ for $i+j>n$), one observes that $D_h v'$ is either horizontal or vertical so that $|D_h v'| = |(D_h)_1 v'| + |(D_h)_2 v'| =: |D_h v'|_1$ (with an obvious notation).

Let $S_h = \bigcup_{i+j=n} C_{i,j}$ be the remaining squares (where, in fact, it is easy to see that $v' = v$), and $\tilde{S}_h = \{1 - h \leq x + y \leq 1 + h\} \supset S_h$. By minimality, we must have that (we use $D_h v = 0$ in $\tilde{S}_h \setminus S_h$, $v = v'$ in S_h)

$$\sqrt{2}h = \int_{\tilde{S}_h} |D_h v| dx = \int_{S_h} |D_h v| dx = \int_{S_h} |D_h v'| dx.$$

It yields that

$$\begin{aligned} 2 = \int_\Omega |D_h v'|_1 dx &= \int_{\Omega \setminus S_h} |D_h v'| dx + \int_{S_h} |D_h v'|_1 dx \\ &= \int_\Omega |D_h v'| dx + \int_{S_h} |D_h v'|_1 - |D_h v'| dx \leq \int_\Omega |D_h v'| dx + (\sqrt{2} - 1) \int_{S_h} |D_h v'| dx. \end{aligned}$$

Hence, we see that in the new triangulation,

$$\int_\Omega |D_h v'| dx \geq 2 - (2 - \sqrt{2})h. \tag{17}$$

This is much larger than the optimal value of $\sqrt{2}$. It means that if we had minimized here the *maximum* of the discrete total variation over the two possible triangulations, such a bad solution would have been ruled out and we would have recovered in the best solution.

We clearly see that we could even do better: we could choose in *each* square $C_{i,j}$ the best triangulation. This is what we describe in the next section.

4.1 Total variation on a square mesh

As before, we use an image domain $\Omega = [0,1]^2$, choose the scale $h = 1/N$, with $N \geq 1$, and discretize Ω into $N \times N$ squares of size $h \times h$. As mentioned above, given such a square mesh[1] in 2D, we can build (2^{N^2}) different triangulations by cutting each square into two triangles, in two possible ways. It is particularly remarkable that in this case, the nodes of the Crouzeix-Raviart spaces associated to these triangulations, which are the middle of the edges, remain the same. As a consequence, given values on the nodes, we can introduce an approximation of the total variation given by the maximum, over all possible triangulations, of the discrete functional (12).

[1] The construction is of course also valid for any quadrangular mesh and just needs a small adaption.

As shown in Figure 5 we need to store values of the image u in the middle of each horizontal and vertical edge as well as in the centers of each square. Therefore we introduce the three index sets $\mathcal{I}_h$, $\mathcal{I}_v$, and $\mathcal{I}_c$ which are given by

$$\begin{aligned}
\mathcal{I}_h &= \left\{\mathbf{i} = ((i+\tfrac{1}{2}), j) : 0 \le i \le N-1,\ 0 \le j \le N\right\},\\
\mathcal{I}_v &= \left\{\mathbf{i} = (i, (j+\tfrac{1}{2})) : 0 \le i \le N,\ 0 \le j \le N-1\right\},\\
\mathcal{I}_c &= \left\{\mathbf{i} = ((i+\tfrac{1}{2}), (j+\tfrac{1}{2})) : 0 \le i \le N-1,\ 0 \le j \le N-1\right\}.
\end{aligned}$$

We also set $\mathcal{I} = \mathcal{I}_h \cup \mathcal{I}_v \cup \mathcal{I}_c$, which refers to the complete set of nodal values. Note that $|\mathcal{I}_h| = |\mathcal{I}_v| = N(N+1)$ and $|\mathcal{I}_c| = N^2$, hence, $|\mathcal{I}| = 3N^2 + 2N$. This shows that the proposed discretization of the total variation increases the number of variables roughly by a factor of three. A more memory efficient (but also more diffusive) version is proposed in section A.

The discrete image image is now given by an image $u \in \mathbb{R}^{\mathcal{I}}$, where we can (by a slight abuse of notation) identify the values of the discrete image with the values of the underlying continuous CR image by means of $u_{\mathbf{i}} = u(\mathbf{i}h)$ for all $\mathbf{i} \in \mathcal{I}$.

Next, we introduce the linear operators $D_1, D_2 : \mathbb{R}^{\mathcal{I}} \mapsto \mathbb{R}^{\mathcal{I}_c \times 4}$, each of them computing per square $\mathbf{i} \in \mathcal{I}_c$ the 4 possible differences out of the 5 nodal values.

$$(D_1 u)_{\mathbf{i}} = \begin{pmatrix} u_{\mathbf{i}} - u_{\mathbf{i}-(\frac{1}{2},0)} \\ u_{\mathbf{i}} - u_{\mathbf{i}-(0,\frac{1}{2})} \\ u_{\mathbf{i}+(\frac{1}{2},0)} - u_{\mathbf{i}} \\ u_{\mathbf{i}+(0,\frac{1}{2})} - u_{\mathbf{i}} \end{pmatrix}, \quad (D_2 u)_{\mathbf{i}} = \begin{pmatrix} u_{\mathbf{i}+(\frac{1}{2},0)} - u_{\mathbf{i}} \\ u_{\mathbf{i}} - u_{\mathbf{i}-(\frac{1}{2},0)} \\ u_{\mathbf{i}} - u_{\mathbf{i}-(0,\frac{1}{2})} \\ u_{\mathbf{i}+(0,\frac{1}{2})} - u_{\mathbf{i}} \end{pmatrix}, \quad \forall \mathbf{i} \in \mathcal{I}_c,$$

where D_1 computes the differences for the first triangulation (the one shown in Figure 5) and D_2 computes the differences of the second triangulation. Moreover, we define the operator $D : \mathbb{R}^{\mathcal{I}} \mapsto \mathbb{R}^{\mathcal{I}_c \times 4 \times 2}$, which simply combines the two preceding operators such that

$$(Du)_{\mathbf{i}} = \left((D_1 u)_{\mathbf{i}}, (D_2 u)_{\mathbf{i}}\right), \quad \forall \mathbf{i} \in \mathcal{I}_c.$$

We are now ready to state the proposed discretization of the total variation, denoted as adaptive Crouzeix-raviart (ACR). It is defined as the energy

$$J_h(u) = h \sum_{\mathbf{i} \in \mathcal{I}_c} f((Du)_{\mathbf{i}}), \tag{18}$$

where the function $f : \mathbb{R}^{4\times 2} \mapsto \mathbb{R}$ is given by

$$f((\xi_{m,n})_{m=1,\dots,4}^{n=1,2}) = \max\left\{\left(\sqrt{\xi_{1,1}^2 + \xi_{2,1}^2} + \sqrt{\xi_{3,1}^2 + \xi_{4,1}^2}\right), \left(\sqrt{\xi_{1,2}^2 + \xi_{2,2}^2} + \sqrt{\xi_{3,2}^2 + \xi_{4,2}^2}\right)\right\}. \tag{19}$$

The function f computes on each square the maximum of the total variation for each of the two possible triangulations. Then, the local contributions are summed over all squares, which gives our proposed adaptive total variation.

In order to apply the proposed ACR discratization of the total variation to image processing problems, we consider generic optimization problems of the form

$$\min_u F(Du) + G(u), \tag{20}$$

where $F(Du) = \lambda J_h(u)$ with $\lambda > 0$ being a regularization parameter. For simplicity we set $h = 1$, because if $h \neq 1$, it can always be lagged into the regularization parameter λ. G is a convex function representing a boundary condition or a data fidelity term. We shall further assume here that the function G is of the form $G(u) = \sum_{\mathbf{i}\in\mathcal{I}} g_{\mathbf{i}}(u_{\mathbf{i}})$.

For solving (20), we consider its saddle-point formulation

$$\min_{u} \max_{\mathbf{p}} \ \langle Du, \mathbf{p}\rangle_P + G(u) - F^*(\mathbf{p}), \tag{21}$$

where $\mathbf{p} = (\mathbf{p}_{\mathbf{i}})_{\mathbf{i}\in\mathcal{I}_c} \in \mathbb{R}^{\mathcal{I}_c\times 4\times 2}$, with $\mathbf{p}_{\mathbf{i}} \in \mathbb{R}^{4\times 2}$ is the dual variable. The function F^* denotes the convex conjugate of the function F and it is given by

$$F^*(\mathbf{p}) = \sum_{\mathbf{i}\in\mathcal{I}_c} f^*(\mathbf{p}_{\mathbf{i}}/\lambda),$$

and f^* refers to the convex conjugate of f as defined in (19). The inner product $\langle\cdot,\cdot\rangle_P$ is naturally given by

$$\langle Du, \mathbf{p}\rangle_P = \sum_{\mathbf{i}\in\mathcal{I}_c}\sum_{m=1}^{4}\sum_{n=1}^{2}(Du)_{\mathbf{i},m,n}\mathbf{p}_{\mathbf{i},m,n}.$$

We will also make use of the adjoint operator $D^* : \mathbb{R}^{\mathcal{I}_c\times 4\times 2} \mapsto \mathbb{R}^{\mathcal{I}}$ which is defined through the identity $\langle Du, \mathbf{p}\rangle_P = \langle u, D^*\mathbf{p}\rangle_U$ with the inner product $\langle\cdot,\cdot\rangle_U$ given by

$$\langle u, D^*\mathbf{p}\rangle_U = \sum_{\mathbf{i}\in\mathcal{I}_c} u_{\mathbf{i}}\,(D^*\mathbf{p})_{\mathbf{i}}.$$

We will also make use of the proximal operators $\operatorname{prox}_{\tau G}(\cdot)$ and $\operatorname{prox}_{\sigma F^*}(\cdot)$, of the functions τG and σF^*. Thanks to their structure, they can be computed solely by means of local operations:

$$\hat{u} = \operatorname{prox}_{\tau G}(\bar{u}) \quad\Longleftrightarrow\quad \hat{u}_{\mathbf{i}} = \operatorname{prox}_{\tau g_{\mathbf{i}}}(\bar{u}_{\mathbf{i}})\ \forall \mathbf{i}\in\mathcal{I}$$

$$\hat{\mathbf{p}} = \operatorname{prox}_{\sigma F^*}(\bar{\mathbf{p}}) \quad\Longleftrightarrow\quad \hat{\mathbf{p}}_{\mathbf{i}} = \arg\min_{\mathbf{p}_{\mathbf{i}}} f^*(\mathbf{p}_{\mathbf{i}}/\lambda) + \frac{1}{2\sigma}\left|\mathbf{p}_{\mathbf{i}} - \bar{\mathbf{p}}_{\mathbf{i}}\right|^2\ \forall \mathbf{i}\in\mathcal{I}_c$$

The proximity operator of the function $f^*(\cdot/\lambda)$ admits a closed form solution, see Appendix B for details. The proximity operators with respect to the functions $g_{\mathbf{i}}$ are usually easy to compute as they represent boundary conditions, or simple 1D functions, see [21] for more information.

We solve the saddle-point problem (21) using the first-order primal-dual algorithm studied in [18, 19]. The algorithm is as follows: Choose any initial $u^0 \in \mathbb{R}^{\mathcal{I}}$ and $\mathbf{p}^0 \in \mathbb{R}^{\mathcal{I}_c\times 4\times 2}$, then for all $k \geq 0$ compute:

$$\begin{cases} u^{k+1} = \operatorname{prox}_{\tau G}\left(u^k - \tau D\mathbf{p}^k\right) \\ \mathbf{p}^{k+1} = \operatorname{prox}_{\sigma F^*}\left(\mathbf{p}^k + \sigma D^*(2u^{k+1} - u^k)\right). \end{cases} \tag{22}$$

It is shown in [18] that the algorithm converges as long as $\tau\sigma L^2 < 1$, where $L = \|D\|$ is the operator norm of the linear operator D. Moreover, its (partial) primal-dual gap converges with rate $O\left(\frac{1}{K}\right)$, where K is the total number of iterations. In case G and/or F^* are strongly convex one can choose optimal (iteration dependent) step sizes such that the algorithm provides improved convergence rates, which in fact are optimal in the sense of lower bounds of first-order methods, see [18, 19, 21] for more details.

5 Numerical experiments

5.1 Comparisons to the state-of-the-art

In order to compare our proposed discretization scheme to the state-of-the-art, we have chosen four different discretization schemes.

First, we will compare to the most simple and most commonly used scheme, which is based on forward differences on a regular grid, as in (2) (see for instance [16]). This scheme suffers from an anisotropy, which is induced by the bias of the forward differences, as shown in Figure 1. In our experiments we will refer to this schemes as finite differences (FD).

Second, we will compare to a upwind forward-backward differences (UFBD) scheme, which borrows ideas from the discretization of Hamilton-Jacobi equations [17]. This scheme adaptively selects between forward and backward differences, based on the sign of the difference and hence is more isotropic but it suffers from the fact that $J(u) \neq J(-u)$.

Third, we will compare to an ℓ_1-type anisotropic total variation that uses non-local finite differences in order to approximate the isotropic total variation [26]. We choose a relatively large neighborhood of 16 to competitive results and hence refer to this scheme as anisotropic finite differences (AFD16).

Finally, we will compare to the recently proposed discretization scheme of L. Condat [23]. The method is based on the dual formulation and uses a more sophisticated application of the pointwise constraint of the dual variable using averaging. In the primal formulation, the scheme can be written as the infimal convolution of three different discrete derivative operators. We will refer to this method as CONDAT.

All algorithms have been implemented in Matlab and are minimized using the first-order primal-dual algorithm [18]. The fastest scheme is FD due to its simplicity. UFBD is slower by about a factor of 2 as it is based on forward and backward differences. ACR and AFD16 have a comparable computational complexity among each other but are slower than FD by about a factor 4. The slowest method is CONDAT which is about a factor of 6 slower than FD. In order to make sure that all algorithms have converged to a solution with sufficient accuracy, we run them for many iterations (> 10000).

5.2 Rotational invariance

In our first experiment, we demonstarte the rotational invariance of the proposed ACR scheme by applying it to the recovery of a straight discontinuity of various orientations $\nu \in \mathbb{S}^1$ in the image domain $\Omega = [0,1]^2$. We discretize Ω at scale $h = 1/N$. Next, we identify the index set $\mathcal{B}$ of boundary points:

$$\mathcal{B} = \{\mathbf{i} \in \mathcal{I} : \mathbf{i}h \in \partial\Omega\}.$$

On the points of the boundary we prescribe the image function according to the equation $u^\diamond_{\mathbf{i}} = \chi_{\{\mathbf{i}h \cdot \nu > a\}}(\mathbf{i}h)$, where $\nu \in \mathbb{S}^1$ is the normal of the discontinuity and $a \in \mathbb{R}$ is set such that the discontinuity passes through the center of the domain.

θ	l	ACR	FD	UFBD	AFD16	CONDAT
$\pi/2$	100.00	**100.00**	**100.00**	**100.00**	97.97	**100.00**
$3\pi/8$	108.24	**108.59**	109.61	108.93	106.04	108.79
$\pi/4$	141.42	**141.42**	142.13	140.01	133.39	140.56

Table 1: This table compares the values of the discrete total variation $J_h(u)$ for the different schemes with the true value of the total variation which is equivalent to the length l of the discontinuity.

In order to recover the discontinuity inside Ω, we solve problem (20) using the data term

$$G(u) = \sum_{\mathbf{i} \in \mathcal{B}} \delta_{\{u_{\mathbf{i}}^{\diamond}\}}(u_{\mathbf{i}}),$$

where $\delta_{\{c\}}(\cdot)$ denotes the indicator function of the singleton c. The proximal map with respect to G is easily computed.

$$\hat{u} = \operatorname{prox}_{\tau G}(\bar{u}) \iff \hat{u}_{\mathbf{i}} = \begin{cases} u_{\mathbf{i}}^{\diamond} & \text{if } \mathbf{i} \in \mathcal{B} \\ \bar{u}_{\mathbf{i}} & \text{else.} \end{cases}.$$

We first demonstrate the property of our proposed ACR discretization scheme to adapt the triangulation to the direction of the discontinuity. For this we set $h = 1/10$, which yields a square grid of 10×10 pixels (squares). We set $\nu = (\cos\theta, \sin\theta)$, with $\theta \in \{0, \pi/4, \pi/2, 3\pi/4\}$ in order to recover discontinuities of the four main orientations. In Figure 7 we show the results for these four main orientations. We plot the continuous image function u, which is piecewise affine on the triangles, and the triangulation itself which is shown in blue. As expected the solution of the problem yields a straight discontinuity with the correct orientation. Observe that the triangulation is automatically adapted to match the orientation of the discontinuity. Moreover, one can also see that in the homogeneous regions the triangulation is ambiguous.

In our second experiment, we repeat the first experiment with orientations $\theta \in \{\pi/2, 3\pi/8, \pi/4\}$ on a larger grid of 100×100 pixels where we set $h = 1$. The aim of this experiment is to evaluate the value of the discrete total variation of the proposed ACR scheme and compare it to the true value of the total variation which is of course given by the length of the discontinuity. Moreover we compare the proposed scheme to existing discretizations and we investigate possible dissipative effects of the different schemes.

In Table 1, we compare the value of the discrete total variation computed by the different schemes. For $\theta = 0$ all scheme except AFD16 give the correct value (up to convergence) of the discontinuity. AFD16 yields the worst results which is due to the systematic anisotropy error inherent to the scheme. As predicted by Proposition 3.3 the proposed ACR scheme is isotropic and hence very successful in recovering the correct value of the total variation for different orientations. Observe that for $\theta = 3\pi/8$ the error is slightly larger which is explained by the fact that the prescribed boundary condition already contains a small error.

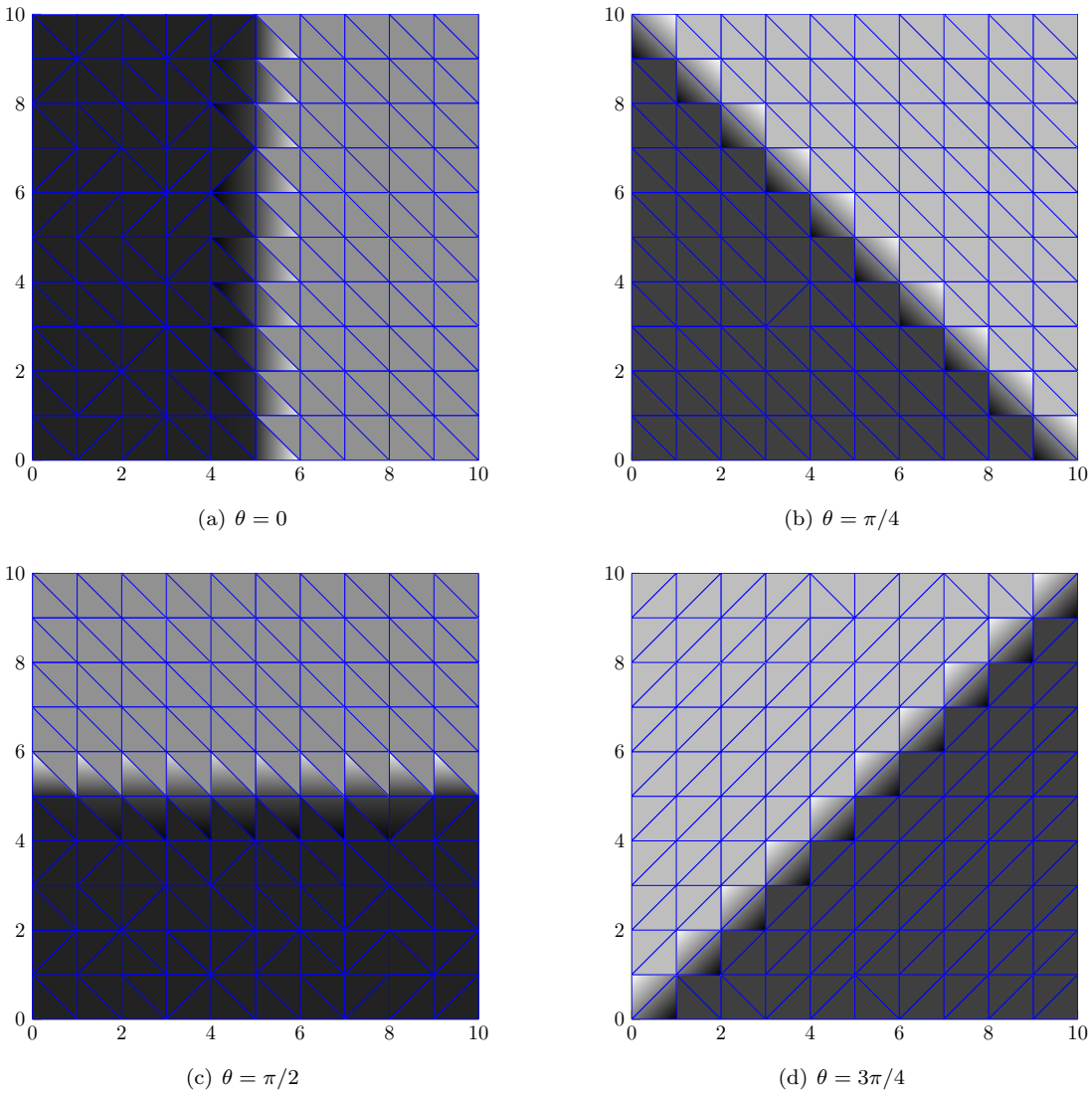

(a) $\theta = 0$ (b) $\theta = \pi/4$

(c) $\theta = \pi/2$ (d) $\theta = 3\pi/4$

Figure 7: Recovery of a discontinuity with normal $\nu = (\cos\theta, \sin\theta)$ on a square grid of 10×10 pixels. We plot the image function which is piecewise affine on the triangles together with the triangulation shown in blue. Observe that the triangles are well aligned with the direction of discontinuity while in homogeneous regions the orientation of the triangles is ambiguous.

In Figure 8 we show the images corresponding to the experiments presented in Table (1). For the proposed ACR scheme we plot an image consisting of center values $u_{i+\frac{1}{2},j+\frac{1}{2}}$ of the squares, for the other schemes, we plot the discrete images which are already part of the scheme. In general all schemes yield sharp discontinuities for $\theta = 0$, which is explained by the alignment of the discontinuity with the grid. FD yields very blurry results for $\theta = \{\pi/4, 3\pi/8\}$, because the forward differences would considerably overestimate the total variation of a sharp discontinuity

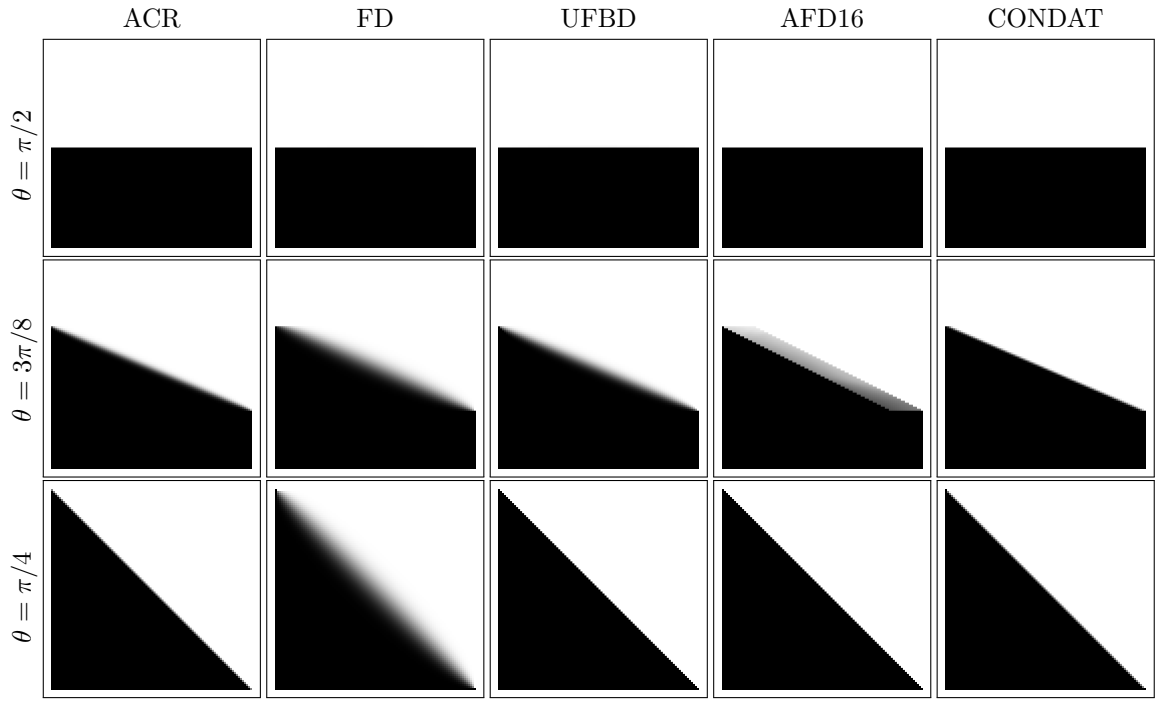

Figure 8: Images corresponding to the experiments of Table 1. Note the significantly more blurry results of FD and the "failure" of AFD16 to recover a straight line with angle $\theta = 3\pi/8$.

(compare Figure 1). AFD16 works well for $\theta = \pi/4$ but produces strong artifacts for $\theta = 3\pi/8$. This is explained by the fact that only orientations which are part of the neighborhood system can be recovered. UFBD yields good results for $\theta = \pi/4$ but gives slightly more blurry results for $\theta = 3\pi/8$. ACR yields good results for all orientations, with a small degree of blur for $\theta = 3\pi/8$. The sharpest transitions are recovered by CONDAT.

5.3 A segmentation problem

In the next experiment we are considering the following geometric minimization problem:

$$\min_u \lambda |Du|(\Omega) + \int_\Omega u(x)(|x| - R)dx, \quad \text{s.t. } 0 \le u(x) \le 1 \ \forall x \in \Omega \tag{23}$$

where $R > 0$ is some parameter and we assume that $0 \in \Omega$. Observe that the level lines of the term $(|x| - R)$ are circles around the origin. Hence, for not too large $\lambda > 0$, the minimizer will be the characteristic function of a disk with radius $r > 0$. Though it can be recovered as the sublevel R of the function in [15, Eq. (39)], for $N = 2$ and $h = \lambda$, we now derive its expression for the reader's convenience.

Using polar coordinates (ρ, θ) the variational problem can be re-written as

$$\min_{r \ge 0} 2\lambda r\pi + \int_0^{2\pi} \int_0^r \rho(\rho - R)d\rho d\theta = 2\pi \min_{r \ge 0} \lambda r + \frac{r^3}{3} - R\frac{r^2}{2}. \tag{24}$$

λ	p	ACR	FD	UFBD	AFD16	CONDAT
25	150.52	150.71	151.80	149.20	146.13	**150.38**
50	143.31	**143.37**	143.65	141.74	138.29	143.40
100	125.66	**125.64**	124.74	122.57	125.08	125.83

Table 2: For a range of different regularization parameters λ, we compute the perimeter $p = 2\pi r$ of the true minimizing disk and compare it to the values of the discrete total variation obtained from different discretization schemes.

The minimal r, if positive, must satisfy $\lambda + r^2 - Rr = 0$, so that:

$$r = \frac{R + \sqrt{R^2 - 4\lambda}}{2}.$$

The disk of radius r solves the problem as long as its energy (24) is nonpositive, since otherwise it is energetically more favorable to choose $r = 0$. The value (24) is less or equal than zero as long as

$$\frac{3R - \sqrt{9R^2 - 48\lambda}}{4} \leq r \leq \frac{3R + \sqrt{9R^2 - 48\lambda}}{4}$$

Comparing this bound with the minimizing radius r, we see that we need to ensure

$$\frac{R + \sqrt{R^2 - 4\lambda}}{2} \leq \frac{3R + \sqrt{9R^2 - 48\lambda}}{4}.$$

Solving for equality we find the upper bound on λ as

$$\lambda = \frac{3}{16}R^2,$$

which corresponds to a radius $r = \frac{3}{4}R$.

The aim of our experiment is now to numerically compute the solution of (23) using our proposed discretization and existing discretization schemes and compare it to the true solution. For comparison we use the value of the total variation which is equivalent of the perimeter $p = 2\pi r$ of the disk. We perform a numerical experiment on a grid of $N \times N$ pixels with $N = 100$, $h = 1$, approximating the image domain Ω and we set $R = N/4 = 25$. The data term in the variational model (20) is given by

$$G(u) = \sum_{\mathbf{i} \in \mathcal{I}_c} u_{\mathbf{i}} w_{\mathbf{i}} + \delta_{[0,1]}(u_{\mathbf{i}}),$$

with segmentation "weight" $w_{\mathbf{i}} = (|\mathbf{i}h| - R)$ and $\delta_{[0,1]}(\cdot)$ denotes the indicator function of the interval $[0, 1]$. Here, we shall assume that the values of the index set are properly shifted such that $0 \in \mathcal{I}_c$ is in the middle of the domain. The proximal map for this data term is easy to compute. It is given by

$$\hat{u} = \operatorname{prox}_{\tau G}(\bar{u}) \iff \hat{u}_{\mathbf{i}} = \max(0, \min(1, \bar{u}_{\mathbf{i}} - \tau w_{\mathbf{i}})), \quad \forall \mathbf{i} \in \mathcal{I}_c$$

From our above computation we know that the problem has a non-trivial minimizer as long as $\lambda \in [0, \frac{3}{16}R^2) \approx [0, 117.18]$.

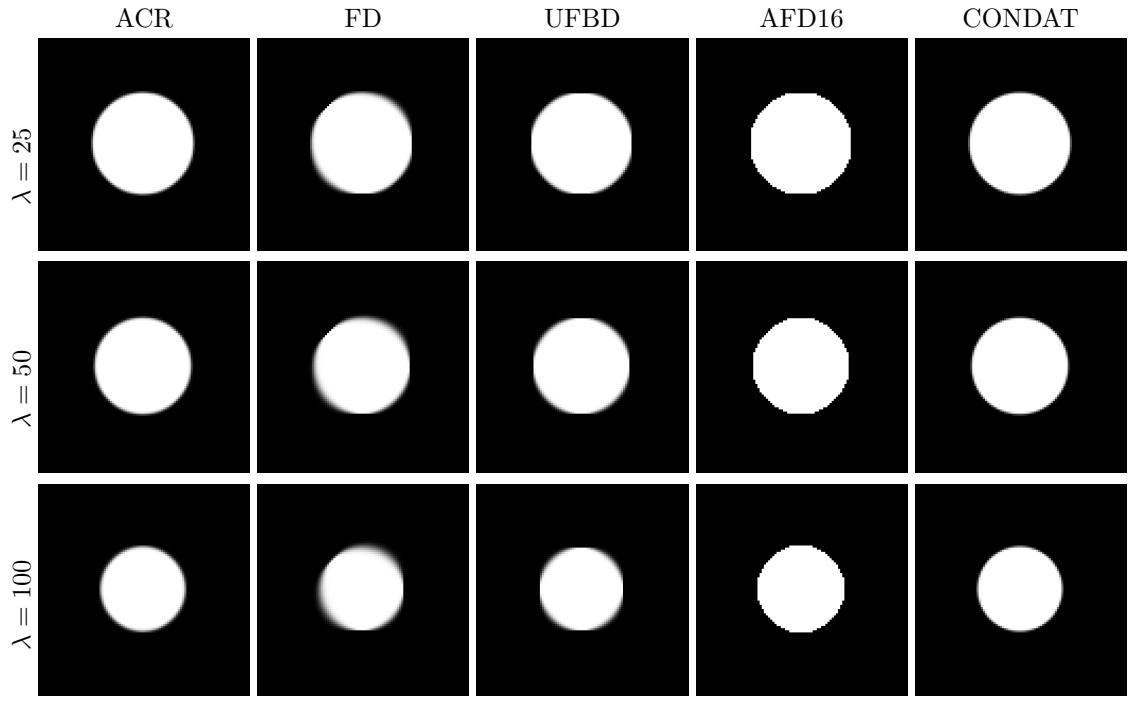

Figure 9: Image scorresponding to the experiments in Table 2. Note the anisotropic behavior of FD and the polygonal behavior of AFD16.

Table 2 compares the values of the discrete total variation to the true perimeter of the disk for different values of the parameter $\lambda \in \{25, 50, 100\}$. From the results we see that both the proposed ACR scheme and CONDAT approximate the true perimeter quite well. FD seems to overestimate the TV for smaller values of λ and underestimate it for larger values of λ. AFD16 and UFBD generally underestimate the TV for all values of λ.

In Figure 9 we provide the images corresponding to the experiments conducted in Table 2. We can observe that ACR provides quite isotropic solutions with slighly blurred interfaces. FD shows the well-known anisotropic smoothing behavior in the four quadrants. UFBD is more isotropic but also shows blurry interfaces. AFD16 provides very sharp interfaces but approximates the disc – as expected – by a 16-polygon. Visually, CONDAT provides the sharpest results.

5.4 Computing the ROF problem for a square

In the next example, we consider the problem of minimizing the ROF problem

$$\min_u \lambda |Du|(\Omega) + \frac{1}{2}\int_\Omega (u(x) - u^\diamond(x))^2 dx,$$

where $u^\diamond(x)$ is the characteristic function of a square, that is $u^\diamond(x) = \chi_{\{[-1,1]^2\}}(x)$. The image domain is set as $\Omega = [-2, 2]^2$ and we are using zero boundary conditions. It is well-known that for any $0 < \lambda < 1/(1 + \sqrt{\pi}/2)$, the solution is given by a lower intensity square with rounded

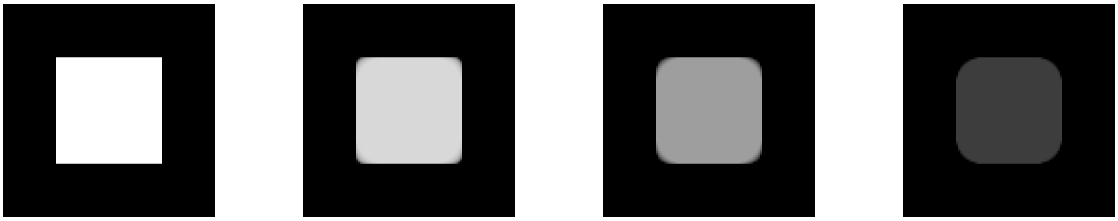

(a) $u^\diamond(x)$ (b) $\lambda = 2$ (c) $\lambda = 5$ (d) $\lambda = 10$

Figure 10: Original square $u^\diamond(x)$, and ground truth solutions $u(x)$ for different values of λ.

λ	ACR	FD	UFBD	AFD16	CONDAT
2	**10.47** / **0.17**	11.77 / 0.26	14.35 / 0.19	18.99 / 0.26	16.38 / 0.19
5	**19.01** / 0.15	22.08 / 0.22	30.54 / 0.18	38.33 / 0.14	23.35 / **0.13**
10	25.21 / 0.09	**23.17** / 0.12	45.85 / 0.10	66.01 / 0.12	25.60 / **0.08**

Table 3: ℓ_1/ℓ_∞-errors between the analytical solutions of the ROF problem and the discrete solutions for different values of the regularization parameter λ.

and blurred corners. The exact solution can be described by an analytical formula, see [1] for more details. Figure 10 plots the characteristic function of the square as well as exact solutions of the regularized squares for $\lambda \in \{2, 5, 10\}$.

In our experiments, we numerically compute the solutions of the regularized squares using different discretizations of the total variation and we compare it to analytical solution. For this, we again set up a grid of $N \times N$ pixels, using $N = 100$ and we set $h = 4/N$ to cover the image domain $\Omega = [-2, 2]^2$. For solving the ROF problem, we use a quadratic data term of the form

$$G(u) = \sum_{\mathbf{i} \in \mathcal{I}_c} (u_\mathbf{i} - u^\diamond_\mathbf{i})^2,$$

where $u^\diamond_\mathbf{i}$ is a point sampled version of the function $u^\diamond(x) = \chi_{\{[-1,1]^2\}}(x)$, as shown in Figure 10 (a).

$$\hat{u} = \operatorname{prox}_{\tau G}(\bar{u}) \iff \hat{u}_\mathbf{i} = \frac{\bar{u}_\mathbf{i} + \tau u^\diamond_\mathbf{i}}{1 + \tau}, \quad \forall \mathbf{i} \in \mathcal{I}_c.$$

In Table 3 we give the ℓ_1 and ℓ_∞ errors between analytical solution and the discrete solutions computed by different discretization schemes of the total variation. The ℓ_1 error captures the global correctness of the solution, i.e. the value of the square, and the ℓ_∞ error captures gross outliers mainly occurring at the corners.

ACR, FD and CONDAT are comparable both in terms the ℓ_1 and ℓ_∞ errors, with most of the time slightly better results for ACR. UFBD is slightly worse in terms of the ℓ_∞ error but has a significantly worse ℓ_1 error. The worst results both in terms of ℓ_1 and ℓ_∞ errors are provided by the AFD16 scheme.

The same behavior can also be seen in the error plots provided in Figure 11. On can clearly see that UFBD and AFD16 have a significant larger global error. The errors at the corners

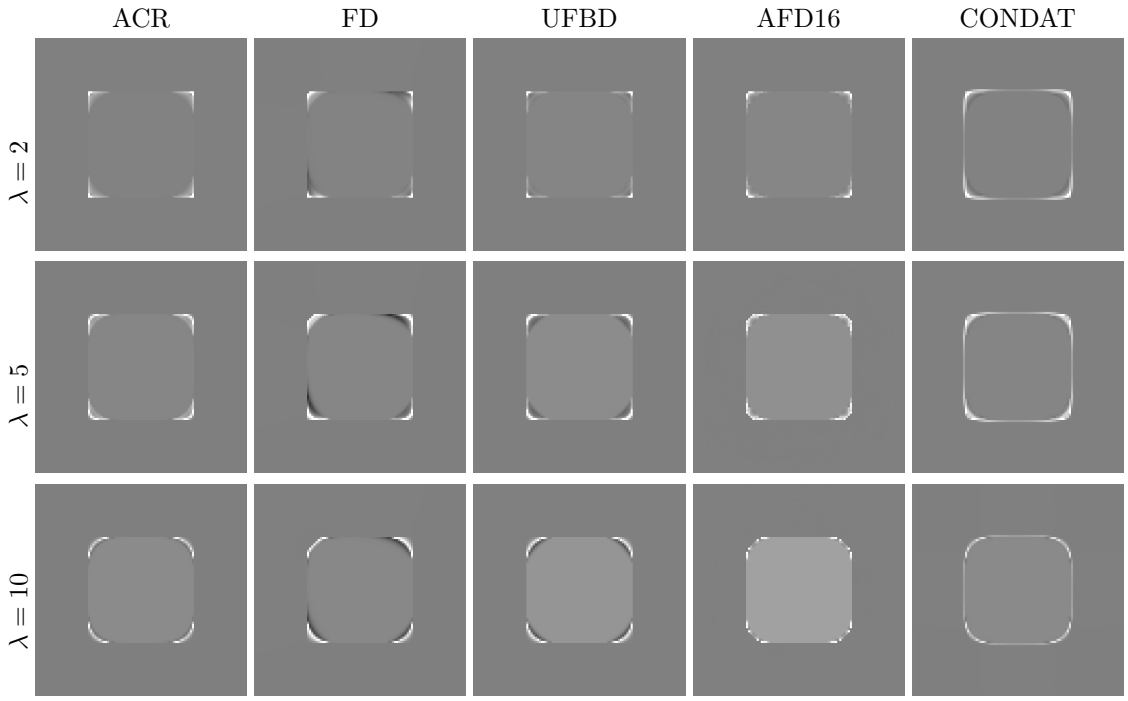

Figure 11: Error plots of the numerical solutions with respect to the analytical solution. For better comparison, the images are truncated to the range $[-0.1, 0.1]$ and gray corresponds to zero. Note the anisotropic behavior of FD and the significantly larger global error of UFBD and AFD16.

slightly differs between the different methods, but one can clearly see that FD has a strongly anisotropic behavior. Interestingly CONDAT also seems to introduce a small error along the edges of the square, which however did not have a large influence to the overall error of the solution.

5.5 An example of image denoising

Finally, we present an examples where we remove the noise of a gray scale image. We use the same discrete ROF model as described in the previous section. Figure 12 shows the noisy clock image together with its ROF denoised images. We also provide detail views of the center pixel values $u_{\mathbf{i}}$ for all $\mathbf{i} \in \mathcal{I}_c$ and a detail view of the corresponding piecewise affine function of the adaptive Crouzeix-Raviart approximation. We also conducted comparisons with other existing discretization schemes, but we omit the results here because they were visually almost identical. The reason is that in case of image denoising the data term is dominating and hence differences in the discretization of the regularizer only have a minor influence on the solution. However, we point out that for more geometric problems, as the problems we have presented in the previous sections, the discretization of the regularizer of course plays a major role.

(a) Noisy image ($\sigma = 0.05$)

(b) Denoised image, $\lambda = 1/25$

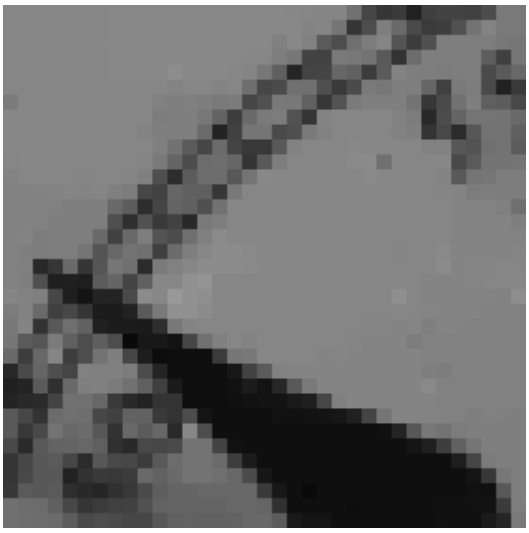

(c) Detail view, pixel values

(d) Detail view, piecewise affine function

Figure 12: Image denoising using the proposed adaptive Crouzeix-Raviart discretization scheme. (a) shows the noisy input image ($\sigma = 0.05$), (b) shows the ROF denoised image, (c) is a detail view of (b) and (d) is the corresponding piecewise affine function of the adaptive Crouzeix-Raviart approximation.

Acknowledgements

The authors would like to thank the Isaac Newton Institute for Mathematical Sciences, Cambridge, for support and hospitality during the programme "Variational methods, new optimisation techniques and new fast numerical algorithms" (Sept.-Oct., 2017), when this work was

undertaken. This work was supported by: EPSRC Grant N. EP/K032208/1. The work of A.C. was partially supported by a grant of the Simons Foundation. T.P. acknowledges support by the Austrian science fund (FWF) under the project EANOI, No. I1148 and the ERC starting grant HOMOVIS, No. 640156.

References

[1] F. Alter, V. Caselles, and Aa Chambolle. Evolution of characteristic functions of convex sets in the plane by the minimizing total variation flow. *Interfaces and Free Boundaries*, 7(1), 2005.

[2] Luigi Ambrosio, Nicola Fusco, and Diego Pallara. *Functions of bounded variation and free discontinuity problems*. Oxford Mathematical Monographs. The Clarendon Press, Oxford University Press, New York, 2000.

[3] Sören Bartels. Total variation minimization with finite elements: convergence and iterative solution. *SIAM J. Numer. Anal.*, 50(3):1162–1180, 2012.

[4] Sören Bartels. Error control and adaptivity for a variational model problem defined on functions of bounded variation. *Math. Comp.*, 84(293):1217–1240, 2015.

[5] Sören Bartels and Marijo Milicevic. Stability and experimental comparison of prototypical iterative schemes for total variation regularized problems. *Comput. Methods Appl. Math.*, 16(3):361–388, 2016.

[6] Sören Bartels, Ricardo H. Nochetto, and Abner J. Salgado. A total variation diminishing interpolation operator and applications. *Math. Comp.*, 84(296):2569–2587, 2015.

[7] Benjamin Berkels, Alexander Effland, and Martin Rumpf. A posteriori error control for the binary Mumford-Shah model. *Math. Comp.*, 86(306):1769–1791, 2017.

[8] Y. Boykov and V. Kolmogorov. Computing geodesics and minimal surfaces via graph cuts. In *Proceedings Ninth IEEE International Conference on Computer Vision*, pages 26–33 vol.1, Oct 2003.

[9] Y. Boykov, V. Kolmogorov, D. Cremers, and A. Delong. An integral solution to surface evolution PDEs via Geo-Cuts. In A. Leonardis, H. Bischof, and A. Pinz, editors, *European Conference on Computer Vision (ECCV)*, volume 3953 of *LNCS*, pages 409–422, Graz, Austria, May 2006. Springer.

[10] Andrea Braides. Γ-*convergence for beginners*, volume 22 of *Oxford Lecture Series in Mathematics and its Applications*. Oxford University Press, Oxford, 2002.

[11] Susanne C. Brenner. Forty years of the Crouzeix-Raviart element. *Numer. Methods Partial Differential Equations*, 31(2):367–396, 2015.

[12] Susanne C. Brenner and L. Ridgway Scott. *The mathematical theory of finite element methods*, volume 15 of *Texts in Applied Mathematics*. Springer, New York, third edition, 2008.

[13] Jian-Feng Cai, Bin Dong, Stanley Osher, and Zuowei Shen. Image restoration: total variation, wavelet frames, and beyond. *J. Amer. Math. Soc.*, 25(4):1033–1089, 2012.

[14] V. Caselles, A. Chambolle, and M. Novaga. The discontinuity set of solutions of the TV denoising problem and some extensions. *Multiscale Model. Simul.*, 6(3):879–894, 2007.

[15] Vicent Caselles and Antonin Chambolle. Anisotropic curvature-driven flow of convex sets. *Nonlinear Anal.*, 65(8):1547–1577, 2006.

[16] A. Chambolle. An algorithm for total variation minimization and applications. *J. Math. Imaging Vision*, 20(1-2):89–97, 2004. Special issue on mathematics and image analysis.

[17] Antonin Chambolle, Stacey E. Levine, and Bradley J. Lucier. An upwind finite-difference method for total variation-based image smoothing. *SIAM J. Imaging Sci.*, 4(1):277–299, 2011.

[18] Antonin Chambolle and Thomas Pock. A first-order primal-dual algorithm for convex problems with applications to imaging. *J. Math. Imaging Vision*, 40(1):120–145, 2011.

[19] Antonin Chambolle and Thomas Pock. On the ergodic convergence rates of a first-order primal-dual algorithm. *Mathematical Programming*, pages 1–35, 2015. (online first).

[20] Antonin Chambolle and Thomas Pock. A remark on accelerated block coordinate descent for computing the proximity operators of a sum of convex functions. *SMAI J. Comput. Math.*, 1:29–54, 2015.

[21] Antonin Chambolle and Thomas Pock. An introduction to continuous optimization for imaging. *Acta Numer.*, 25:161–319, 2016.

[22] Antonin Chambolle, Pauline Tan, and Samuel Vaiter. Accelerated alternating descent methods for Dykstra-like problems. *Journal of Mathematical Imaging and Vision*, Mar 2017.

[23] Laurent Condat. Discrete total variation: new definition and minimization. *SIAM J. Imaging Sci.*, 10(3):1258–1290, 2017.

[24] M. Crouzeix and P.-A. Raviart. Conforming and nonconforming finite element methods for solving the stationary Stokes equations. I. *Rev. Française Automat. Informat. Recherche Opérationnelle Sér. Rouge*, 7(R-3):33–75, 1973.

[25] Gianni Dal Maso. *An introduction to* Γ*-convergence*, volume 8 of *Progress in Nonlinear Differential Equations and their Applications*. Birkhäuser Boston, Inc., Boston, MA, 1993.

[26] Jérôme Darbon and Marc Sigelle. Exact optimization of discrete constrained total variation minimization problems. In *Combinatorial image analysis*, volume 3322 of *Lecture Notes in Comput. Sci.*, pages 548–557. Springer, Berlin, 2004.

[27] Daniele A. Di Pietro and Simon Lemaire. An extension of the Crouzeix-Raviart space to general meshes with application to quasi-incompressible linear elasticity and Stokes flow. *Math. Comp.*, 84(291):1–31, 2015.

[28] C. M. Elliott and S. A. Smitheman. Numerical analysis of the TV regularization and H^{-1} fidelity model for decomposing an image into cartoon plus texture. *IMA J. Numer. Anal.*, 29(3):651–689, 2009.

[29] Xiaobing Feng and Andreas Prohl. Analysis of total variation flow and its finite element approximations. *M2AN Math. Model. Numer. Anal.*, 37(3):533–556, 2003.

[30] Xiaobing Feng, Markus von Oehsen, and Andreas Prohl. Rate of convergence of regularization procedures and finite element approximations for the total variation flow. *Numer. Math.*, 100(3):441–456, 2005.

[31] Duvan Henao, Carlos Mora-Corral, and Xianmin Xu. A numerical study of void coalescence and fracture in nonlinear elasticity. *Comput. Methods Appl. Mech. Engrg.*, 303:163–184, 2016.

[32] Clemens Kirisits, Christiane Pöschl, Elena Resmerita, and Otmar Scherzer. Finite-dimensional approximation of convex regularization via hexagonal pixel grids. *Appl. Anal.*, 94(3):612–636, 2015.

[33] Ming-Jun Lai, Bradley Lucier, and Jingyue Wang. *The Convergence of a Central-Difference Discretization of Rudin-Osher-Fatemi Model for Image Denoising*, pages 514–526. Springer Berlin Heidelberg, Berlin, Heidelberg, 2009.

[34] Ming-Jun Lai and Leopold Matamba Messi. Piecewise linear approximation of the continuous Rudin-Osher-Fatemi model for image denoising. *SIAM J. Numer. Anal.*, 50(5):2446–2466, 2012.

[35] Christoph Ortner. Nonconforming finite-element discretization of convex variational problems. *IMA J. Numer. Anal.*, 31(3):847–864, 2011.

[36] Christoph Ortner and Dirk Praetorius. On the convergence of adaptive nonconforming finite element methods for a class of convex variational problems. *SIAM J. Numer. Anal.*, 49(1):346–367, 2011.

[37] P.-A. Raviart and J. M. Thomas. A mixed finite element method for 2nd order elliptic problems. pages 292–315. Lecture Notes in Math., Vol. 606, 1977.

[38] Carsten Rother, Vladimir Kolmogorov, and Andrew Blake. "GrabCut": Interactive foreground extraction using iterated graph cuts. *ACM Trans. Graph.*, 23(3):309–314, August 2004.

[39] L. Rudin, S. J. Osher, and E. Fatemi. Nonlinear total variation based noise removal algorithms. *Physica D*, 60:259–268, 1992. [also in *Experimental Mathematics: Computational Issues in Nonlinear Science* (Proc. Los Alamos Conf. 1991)].

[40] Jingyue Wang and Bradley J. Lucier. Error bounds for finite-difference methods for Rudin-Osher-Fatemi image smoothing. *SIAM J. Numer. Anal.*, 49(2):845–868, 2011.

[41] Xianmin Xu and Duvan Henao. An efficient numerical method for cavitation in nonlinear elasticity. *Math. Models Methods Appl. Sci.*, 21(8):1733–1760, 2011.

A A variant with one node per pixel

For imaging application, one drawback of our approach could be the need to introduce more nodes in the representation than the number of pixels.

Given a (grey-level) $n \times m$ image $(u_{i,j})_{i=1,\dots,n}^{j=1,\dots,m}$ (to simplify, we assume that the scale $h = 1$ in this section), even if one rotates the grid by 45° and considers the pixels (i, j) as centers of edges of larger squares (for instance, $(1,1), (1,2), (2,1), (2,2)$ would be the centers of the edges of the square $[(3/2, 1/2), (5/2, 3/2), (3/2, 5/2), (1/2, 3/2)]$), one still needs to introduce an additional node in the center of each square (in the above example, at $(3/2, 3/2)$) and introduce fictitious values $u_{i+1/2,j+1/2}$ (i, j both even or both odd) at these nodes. On average, this increases the dimension of the problems by roughly 50%.

Unfortunately, it seems there is no simple strategy to eliminate this additional node. To illustrate this issue, let us first concentrate on one square. We consider the four vertices $\{0,1\}^2$ as the middle points of the edges of the square (of area 2)

$$C = \left[\left(\tfrac{1}{2}, -\tfrac{1}{2}\right), \left(\tfrac{3}{2}, \tfrac{1}{2}\right), \left(\tfrac{1}{2}, \tfrac{3}{2}\right), \left(-\tfrac{1}{2}, \tfrac{1}{2}\right)\right]$$

and a fifth vertex in $(1/2, 1/2)$ in the middle, which is the middle of both the vertical and horizontal edges cutting the square into two halves. Then, given the values $u_{\alpha,\beta} := u(\alpha, \beta)$, $(\alpha, \beta) \in \{0,1\}^2$, and c the value at the center, the Crouzeix-Raviart total variation inside the square is

$$\max\Big\{\sqrt{2}\sqrt{(u_{00}-c)^2+(u_{10}-c)^2}+\sqrt{2}\sqrt{(u_{11}-c)^2+(u_{01}-c)^2},\\ \sqrt{2}\sqrt{(u_{00}-c)^2+(u_{01}-c)^2}+\sqrt{2}\sqrt{(u_{11}-c)^2+(u_{10}-c)^2}\Big\}.$$

(Each gradient norm is multiplied by the area 1 of the corresponding triangle, and we have used that the distance between a vertex of the cube and the center is $1/\sqrt{2}$.) A possibility to eliminate c is to minimize this quantity with respect to c. In the "inpainting" problems of Fig. 8, this would give the same results (since this is precisely what is done automatically by the minimization in

this case). Unfortunately we have, at this point, no idea of how to solve this problem explicitly. It means that to compute the "proximity" operator of the corresponding energy on a whole image, we need to solve subproblems which keep the additional central variable.

A simpler possibility is to first optimize with respect to the value c and then, afterwards, pick the best orientation. In that case, one needs to solve

$$\sqrt{2}\max\Big\{\min_c \sqrt{(u_{00}-c)^2+(u_{10}-c)^2}+\sqrt{(u_{11}-c)^2+(u_{01}-c)^2},\\ \min_c \sqrt{(u_{00}-c)^2+(u_{01}-c)^2}+\sqrt{(u_{11}-c)^2+(u_{10}-c)^2},\Big\}.$$

A careful analysis shows that this value is given by the function

$$J^4((u_{00},u_{10},u_{01},u_{11})) := \\ \sqrt{2}\max\Big\{\sqrt{(u_{11}-u_{00})^2+(u_{10}-u_{01})^2},\sqrt{(u_{01}-u_{00})^2+(u_{11}-u_{10})^2},\\ \sqrt{(u_{10}-u_{00})^2+(u_{11}-u_{01})^2}\Big\}. \quad (25)$$

One can use (25) to define, for an image u defined by its pixel values $(u_{i,j})_{i=1,\dots,n}^{j=1,\dots,m}$, a discrete total variation as

$$J(u) := \sum_{(i,j)\text{ even}} J^4((u_{i,j},u_{i+1,j},u_{i,j+1},u_{i+1,j+1})) + \sum_{(i,j)\text{ odd}} J^4((u_{i,j},u_{i+1,j},u_{i,j+1},u_{i+1,j+1})). \quad (26)$$

We remark this is a variant of the energy defined in [20] (see also [22] for a theoretical study), which can be optimized by an efficient alternating descent method as soon as one knows how to solve explicitly the subproblems given by the proximity operator of J^4, on each square.

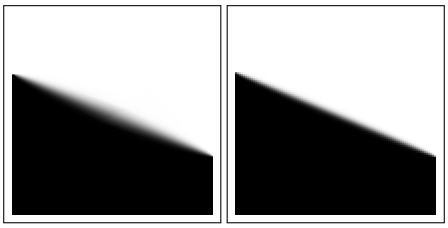

Figure 13: Left: the variant (26), right: the ACR result of Fig. 8.

Unfortunately, our implementation shows that it does not perform as well as the ACR technique introduced in this paper. Figure 13 compares this to the ACR result in Fig. 8: we obtain a very diffusive solution, with practically no improvement over a non-optimized Crouzeix Raviart implementation.

On the other hand, as is expected, this approximation (which in any case is still based on a hidden, underlying Crouzeix-Raviart discretization), yields to a quite precise approximation of the energy and is a reasonable regularizer for standard inverse problems, *cf.* Fig. 14.

Figure 14: Left: original "clock" image, middle: with a Gaussian blur of std. dev. 1.5 and a 1% Gaussian noise, right: TV-regularised deblurred image with (26).

B The proximity operator of (19)

We describe in this Section how to implement the proximity operator of the function f in (19). The problem we need to solve is as follows, given $\bar{\xi} = (\bar{\xi}_{mn})_{m=1,\dots,4}^{n=1,2} \in \mathbb{R}^{4\times 2}$ and $\tau > 0$:

$$\min_{\xi=(\xi_{mn})_{m=1,\dots,4}^{n=1,2}\in\mathbb{R}^{4\times 2}} f(\xi) + \frac{1}{2\tau}\|\xi - \bar{\xi}\|^2. \tag{27}$$

We call $\text{prox}_{\tau f}(\bar{\xi})$ the solution of (27). We recall that the prox of the convex conjugate f^* is also easily recovered, once (27) is solved, using Moreau's identity:

$$x = \text{prox}_{\tau f}(x) + \tau \text{prox}_{\frac{1}{\tau} f^*}(\tfrac{x}{\tau}).$$

To solve (27) we first make the following obvious observation: denoting

$$\begin{aligned}
x_1 &= \sqrt{\xi_{1,1}^2 + \xi_{2,1}^2}, \quad (\xi_{1,1}, \xi_{2,1})^T = x_1\eta_1,\\
x_2 &= \sqrt{\xi_{3,1}^2 + \xi_{4,1}^2}, \quad (\xi_{3,1}, \xi_{4,1})^T = x_2\eta_2,\\
x_3 &= \sqrt{\xi_{1,2}^2 + \xi_{2,2}^2}, \quad (\xi_{1,2}, \xi_{2,2})^T = x_3\eta_3,\\
x_4 &= \sqrt{\xi_{3,2}^2 + \xi_{4,2}^2}, \quad (\xi_{3,2}, \xi_{4,2})^T = x_4\eta_4,
\end{aligned}$$

(and the same for $\bar{\xi}$), it is equivalent to solve:

$$\min_{(x_i)\geq 0,(\eta_i)} \max\{|x_1| + |x_2|, |x_3| + |x_4|\} + \frac{1}{2\tau}\sum_{i=1}^{4} |x_i\eta_i - \bar{x}_i\bar{\eta}_i|^2.$$

We obtain at the minimum that $\eta_i = \bar{\eta}_i$, $i = 1, \dots, 4$ and the problem boils down to

$$\min_{x=(x_i)_{i=1}^4\in\mathbb{R}_+^4} \max\{|x_1| + |x_2|, |x_3| + |x_4|\} + \frac{1}{2\tau}|x - \bar{x}|^2$$

where $|x-\bar{x}|^2 = \sum_{i=1}^4 |x_i - \bar{x}_i|^2$. Remark that here, $\bar{x}_i \geq 0$ and it is equivalent to look for $x \in \mathbb{R}^4_+$ or in $\mathbb{R}^4$.

We now explain how to solve this 4-dimensional convex problem. We can rewrite it as

$$\min_x \max_{\substack{\mu_{12}+\mu_{34}=1 \\ \mu_{12}\geq 0, \mu_{34}\geq 0}} \mu_{12}(|x_1|+|x_2|) + \mu_{34}(|x_3|+|x_4|) + \frac{1}{2\tau}|x-\bar{x}|^2$$

and then we exchange min and max. We obtain 4 problems of the form

$$\min_{x_1} \mu_{12}|x_1| + \frac{1}{2\tau}|x_1 - \bar{x}_1|^2.$$

This is well known to be solved by $x_1 = (\bar{x}_1 - \tau\mu_{12})^+$ and with value

$$\mu_{12}(\bar{x}_1 - \tau\mu_{12})^+ + \frac{1}{2\tau}\begin{cases} |\bar{x}_1|^2 & \text{if } \bar{x}_1 \leq \tau\mu_{12} \\ |\tau\mu_{12}|^2 & \text{else.} \end{cases}$$

When $\bar{x}_1 \leq \tau\mu_{12}$, this is $|\bar{x}_1|^2/(2\tau)$, otherwise

$$\mu_{12}\bar{x}_1 - \frac{\tau}{2}|\mu_{12}|^2 = \frac{1}{2\tau}|\bar{x}_1|^2 - \frac{1}{2\tau}|\bar{x}_1 - \tau\mu_{12}|^2.$$

We end up with the dual problem

$$\max_{\substack{\mu_{12}+\mu_{34}=1 \\ \mu_{12}\geq 0, \mu_{34}\geq 0}} \frac{1}{2\tau}\Big(\sum_{i=1}^4 |\bar{x}_i|^2 - \big(|(\bar{x}_1 - \tau\mu_{12})^+|^2 + |(\bar{x}_2 - \tau\mu_{12})^+|^2 \\ + |(\bar{x}_3 - \tau\mu_{34})^+|^2 + |(\bar{x}_4 - \tau\mu_{34})^+|^2\big)\Big),$$

whose optimality reads, if $0 < \mu_{12} < 1$,

$$(\bar{x}_1 - \tau\mu_{12})^+ + (\bar{x}_2 - \tau\mu_{12})^+ = (\bar{x}_3 - \tau\mu_{34})^+ + (\bar{x}_4 - \tau\mu_{34})^+$$

with $\mu_{34} = 1 - \mu_{12}$.

Without loss of generality, assume that $\bar{x}_2 \geq \bar{x}_1$ and $\bar{x}_4 \geq \bar{x}_3$. We recast the problem as

$$\min_{0\leq\mu\leq 1} |(\bar{x}_1 - \tau\mu)^+|^2 + |(\bar{x}_2 - \tau\mu)^+|^2 + |(\bar{x}_3 - \tau + \tau\mu)^+|^2 + |(\bar{x}_4 - \tau + \tau\mu)^+|^2$$

by letting $\mu := \mu_{12}$ and $\mu_{34} = 1 - \mu$.

By convexity of the objective, $\mu \in [0,1]$ is optimal if and only if:

$$\begin{cases} (\bar{x}_1 - \tau\mu)^+ + (\bar{x}_2 - \tau\mu)^+ - (\bar{x}_3 - \tau + \tau\mu)^+ - (\bar{x}_4 - \tau + \tau\mu)^+ \leq 0 & \text{if } \mu < 1\,; \\ (\bar{x}_1 - \tau\mu)^+ + (\bar{x}_2 - \tau\mu)^+ - (\bar{x}_3 - \tau + \tau\mu)^+ - (\bar{x}_4 - \tau + \tau\mu)^+ \geq 0 & \text{if } \mu > 0. \end{cases} \tag{28}$$

Hence, one sees that if one knows which term are positive in the above sums, μ is found by solving the above equations with "$= 0$" instead of "$\geq$ / ≤ 0" and then projecting the value onto the interval $[0,1]$. For instance, if all values are positive,

$$\mu = \left(0 \vee \frac{\bar{x}_1 + \bar{x}_2 - \bar{x}_3 - \bar{x}_4 + 2\tau}{4\tau}\right) \wedge 1. \tag{29}$$

Whenever $\mu \in (0,1)$, of course, (28) reads

$$(\bar{x}_1 - \tau\mu)^+ + (\bar{x}_2 - \tau\mu)^+ = (\bar{x}_3 - \tau + \tau\mu)^+ + (\bar{x}_4 - \tau + \tau\mu)^+. \tag{30}$$

Hence, the problem is solved by exhaustion of the following cases:

1. if $\bar{x}_2 + \bar{x}_4 \leq \tau$, then clearly one can find $\mu \in [0,1]$ such that all terms of the sums in (28) are zero, hence the solution is $x_1 = x_2 = x_3 = x_4 = 0$.

2. if $\bar{x}_2 + \bar{x}_4 > \tau$ then:

   (a) either *both* $\bar{x}_2 - \tau\mu > 0$ and $\bar{x}_4 - \tau + \tau\mu > 0$,

   (b) or one side of (30) is zero so that one must be in a case of strict inequality in (28), and $\mu \in \{0,1\}$.

   The second case 2b can be first easily eliminated by checking whether $\mu = 0$ or $\mu = 1$ is a solution of the optimality condition: one has

   $$\bar{x}_1 + \bar{x}_2 \leq (\bar{x}_3 - \tau)^+ + (\bar{x}_4 - \tau)^+ \;\Leftrightarrow\; \mu = 0,$$
   $$(\bar{x}_1 - \tau)^+ + (\bar{x}_2 - \tau)^+ \geq \bar{x}_3 + \bar{x}_4 \;\Leftrightarrow\; \mu = 1.$$

3. Otherwise, we must be in the first case 2a, where $\bar{x}_2 - \tau\mu > 0$ and $\bar{x}_4 - \tau + \tau\mu > 0$, equality (30) holds, and which is then split into four possible cases:

   (a) μ given by (29), and $\bar{x}_1 \geq \tau\mu$, $\bar{x}_3 \geq \tau(1-\mu)$, then $x_1 = \bar{x}_1 - \tau\mu$, $x_2 = \bar{x}_2 - \tau\mu$, $x_3 = \bar{x}_3 - \tau(1-\mu)$, $x_4 = \bar{x}_4 - \tau(1-\mu)$.

   (b) $\mu = \frac{\bar{x}_1 + \bar{x}_2 - \bar{x}_4 + \tau}{3\tau}$ and $\bar{x}_1 \geq \tau\mu$, $\bar{x}_3 \leq \tau(1-\mu)$, $\bar{x}_3 \geq \tau(1-\mu)$, then $x_1 = \bar{x}_1 - \tau\mu$, $x_2 = \bar{x}_2 - \tau\mu$, $x_3 = 0$, $x_4 = \bar{x}_4 - \tau(1-\mu)$;

   (c) $\mu = \frac{\bar{x}_2 - \bar{x}_3 - \bar{x}_4 + 2\tau}{3\tau}$ and $\bar{x}_1 \leq \tau\mu$, $\bar{x}_2 \geq \tau\mu$, $\bar{x}_3 \geq \tau(1-\mu)$, then $x_1 = 0$, $x_2 = \bar{x}_2 - \tau\mu$, $x_3 = \bar{x}_3 - \tau(1-\mu)$, $x_4 = \bar{x}_4 - \tau(1-\mu)$;

   (d) $\mu = \frac{\bar{x}_2 - \bar{x}_4 + \tau}{2\tau}$ if all the previous cases fail to hold, and then $x_1 = x_3 = 0$, $x_2 = \bar{x}_2 - \tau\mu$, $x_4 = \bar{x}_4 - \tau(1-\mu)$;